



ELSEVIER

Contents lists available at ScienceDirect

Experimental Thermal and Fluid Science

journal homepage: www.elsevier.com/locate/etfs

Two-dimensional integral turbulent scales in compression wave in a canal

Xinqian Leng, Hubert Chanson*

The University of Queensland, School of Civil Engineering, Brisbane QLD 4072, Australia

ARTICLE INFO

Keywords:

Compression waves
Unsteady turbulence
Space-time correlations
Turbulent time and length scales
Acoustic Doppler velocimetry

ABSTRACT

A compression wave in a canal is an unsteady motion characterised by a rapid rise of water surface elevation, resulting in an unsteady turbulent flow. In the present study, the hydrodynamics of unsteady compression wave flows were experimentally investigated using an array of two profiling velocimeters, sampled simultaneously. The two-dimensional cross-correlation data in the y-z plane, formed by the two sampling profiles, showed the existence of large scale coherent structures underneath the free-surface, resembling the shape of hairpin vortex. The length scales tended to increase during and after the compression wave passage compared to those during the initially steady flows. Both strain rate and vorticity showed larger values at lower water column near the channel bed, and during the rapid deceleration phase associated with immediate wave passage. The propagation of the compression wave was a dynamically-active process, with large scale transient coherent motions, vortical structures and intensive turbulent mixing occurring underneath.

1. Introduction

A transition from a rapid to fluvial motion in an open channel is called a hydraulic jump. A related flow is a hydraulic jump in translation or compression wave. In nature, a hydraulic jump in translation may occur in a small number of rivers and estuaries with large tidal range, low freshwater level and a funnel-shaped river mouth [33,36,9]. Fig. 1 illustrates such a compression wave called tidal bore, in the Qiantang River (China) at nearly 110 km upstream of the river mouth. A related geophysical process is the in-river tsunami-induced bore ([31,1,11]. The propagation of a compression wave in a canal is an unsteady turbulent process, with intense shear and mixing underneath. The strength and shape of the bore is characterised by its Froude number Fr_1 defined as:

$$Fr_1 = \frac{V_1 + U}{\sqrt{g \frac{A_1}{B_1}}} \quad (1)$$

where V_1 is the initial flow velocity positive downstream, U is the compression wave celerity positive upstream, g is the gravitational acceleration, A_1 and B_1 are respectively the cross-sectional area and the free-surface width. When $1 < Fr_1 < 1.3$ – 1.4 , the bore is undular, characterised by a smooth free-surface rise and a train of secondary, quasi-periodic waves [35,20]. For $1.4 < Fr_1$, the bore is breaking with a turbulent breaking roller and energetic white water splashes (Fig. 1) [18,22]. The roller is characterised by an abrupt free-surface rise, a two-

phase flow region with air-water interactions, large-scale vortical structures and intensive energy dissipation [21,8].

Experimental studies of compression wave in canal may be dated back to Bazin [3], Favre [14], and Benet and Cunge [5], who performed classical experiments with visual observations. More recent physical studies used advanced velocity sampling equipment with high temporal resolutions, such as a particle imaging velocimetry (PIV) and acoustic Doppler velocimetry (ADV) [18,20,23].

Herein, new experiments were conducted to study the two-dimensional unsteady turbulence characteristics of compression waves in a systematic manner under controlled flow conditions. Two Vectrino II Profilers were operated simultaneously, and turbulent time and length scales of large transient coherent structures were computed, as well as space-time correlations, in the transverse and vertical directions. Unsteady measurements with an array of two Profilers provided new insights into the turbulence underneath the hydraulic jump in translation.

2. Physical modelling

2.1. Experimental facility

New experiments were conducted in a 19 m long, 0.7 m wide tilting flume, previous used by Leng and Chanson [22,23]. The flume was rectangular prismatic, made of glass sidewalls and smooth PVC bed with an adjustable bed slope. The water discharge was supplied by an

* Corresponding author.

E-mail address: h.chanson@uq.edu.au (H. Chanson).



Fig. 1. Photograph of the breaking tidal bore of the Qiantang River at Jiuxi, China on 20 September 2016 – Bore propagation from left to right.

upstream water tank through a smooth convergent intake into the test section. A magneto flowmeter was used to measure the water discharge down to an accuracy of $10^{-5} \text{ m}^3/\text{s}$, and checked against drink depth data (Fig. 2A). A fast-closing Tainter gate was located near the downstream end at $x = 18.1 \text{ m}$, where x is the longitudinal distance from the upstream end (Fig. 2A). After rapidly closure in less than 0.2 s, the Tainter gate generated a compression wave which propagated upstream. The definition sketch of the flume, experimental apertures and mounting of instrumentations is shown in Fig. 2.

2.2. Instrumentation

In steady flows, the water elevation was recorded with pointer gauges. Unsteady water elevations were measured with acoustic displacement meters (ADMs). A Microsonic™ Mic + 35/IU/TC unit was located at $x = 18.17 \text{ m}$ immediately downstream of the Tainter gate. Nine Microsonic™ Mic + 25/IU/TC ADMs were spaced along the channel at $x = 17.81 \text{ m}$, 17.41 m , 14.96 m , 12.46 m , 9.96 m , 8.5 m , 6.96 m , 3.96 m and 1.96 m , all locations being upstream of the Tainter gate.

Two profiling velocimeters were deployed herein. Both instruments were Nortek™ acoustic Doppler velocimeter (ADV) Vectrino II Profilers. (Note that the profiler units were not re-calibrated following the manufacturer's 2016 worldwide recall.) One was equipped with a fixed downward looking head. The other one was equipped with a flexible head, which was mounted side-looking in the present study. The former is referred to as Profiler 1, while the side-looking Profiler is called Profiler 2. The Vectrino II Profiler is a high-resolution acoustic Doppler velocimeter used to measure three-dimensional water velocity [30]. The measurement technology is based upon coherent Doppler processing [38]. There are however known issues with the Vectrino II Profiler, including inaccurate estimation of time-averaged velocity at certain positions and wrong estimation of velocity variances at the profile “weak spots” [12,38,23,13]. In the present study, both Profilers were configured to quasi-simultaneously sample the velocity at 100 Hz for 35 sampling points in a 35 mm profile (Fig. 2B). The sampling volume (or profile) of Profiler 1 was in the vertical direction, located 40 mm below the emitter, whereas the sampling volume of Profiler 2 was in the transverse direction, located 40 mm beside the emitter. Fig. 2A shows sketches of the two Profilers with the coordinate system and Fig. 2C presents the array of sampling profiles. Profilers 1 and 2 were mounted at $x = 8.5 \text{ m}$ and 8.425 m , respectively. The velocity

range was $\pm 1.0 \text{ m/s}$ or $\pm 1.5 \text{ m/s}$. Both Profilers were sampled simultaneously with the ADMs at 100 Hz and synchronised within $\pm 1 \text{ ms}$. The vertical displacement of the Profilers was controlled by a fine-adjustment screwdrive traverse and recorded using a Mitutoyo™ digimatic scale unit with an accuracy of less than 0.025 mm. The distance from the emitter to the channel bed was checked against the built-in bottom check function of the Vectrino II Profiler [30].

The output data of the Profilers were saved as MATLAB files. Steady flow data were post-processed by the MATLAB program VTMT version 1.1, designed and written by Jan Becker from Federal Waterways Engineering and Research Institute [4]. In steady flows, the post-processing included the removal of data with average correlation values less than 60% and average signal to noise ratio less than 5 dB. In addition, the phase-space thresholding technique developed by Goring and Nikora [16] was applied to remove spurious points in the data set. In the unsteady flows, the above post-processing technique was not applicable [29], *Person. Comm.*, [7,8] and raw data was used directly for analysis.

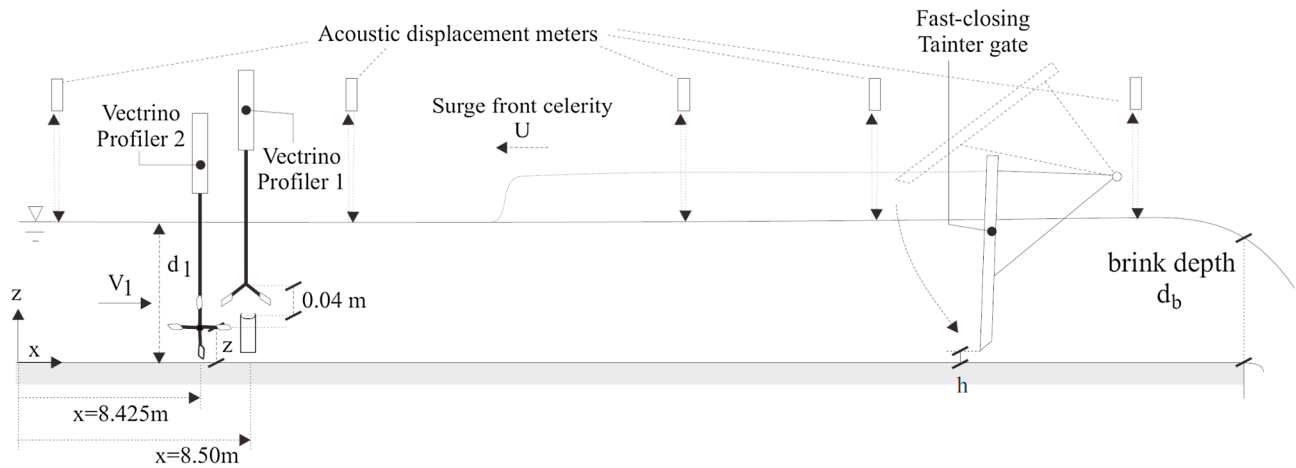
2.3. Experimental flow conditions

Preliminary experiments were undertaken with the Profiler 1 or Profiler 2 alone. The detailed results are reported in Leng and Chanson [24]. Herein the focus is on the unsteady flow experiments conducted using simultaneously the two Profilers. The experimental flow conditions were chosen based upon the preliminary results. Table 1 summarises the flow conditions, where S_0 is the bed slope, Q is the initially steady water discharge, d_1 is the initial water depth at $x = 8.5 \text{ m}$, and h is the Tainter gate opening after closure (Fig. 2A). For each sampling location, the experiments were repeated 25 times, and the results were ensemble-averaged.

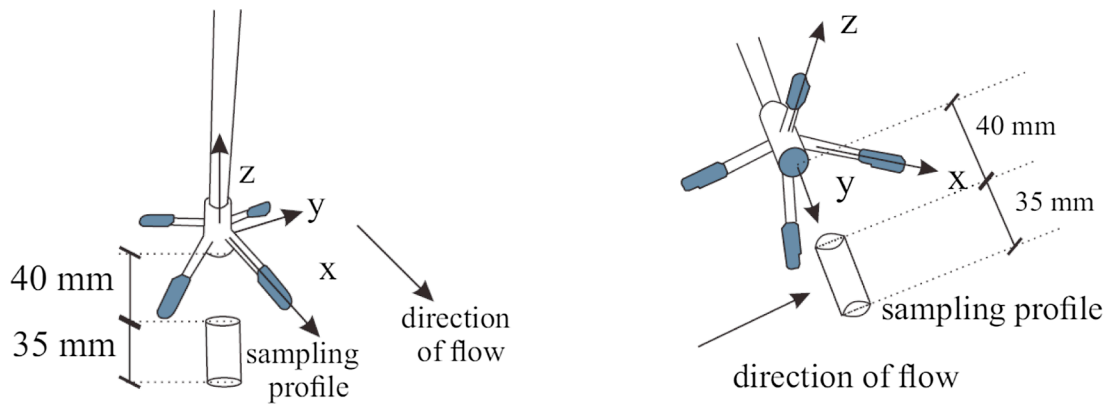
3. Probe array data processing

3.1. Cross-correlation and turbulent time scales

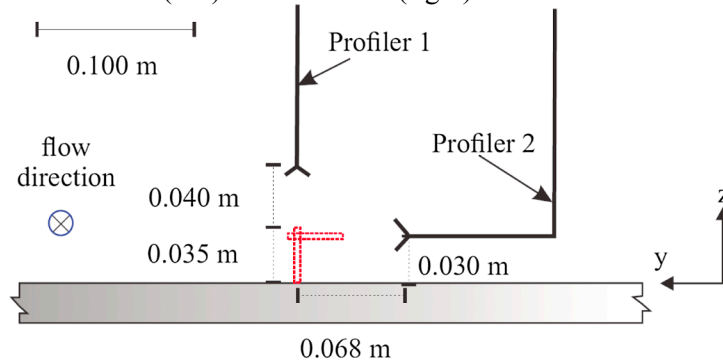
The cross-correlation functions $R_{y,z,i}$ were calculated between the velocity signals of the two Profilers to examine the turbulent scales in the plane formed by the two sampling profiles, with i denoting the velocity component: $i = x, y, z$, (Fig. 3). Calculations were carried out by cross-correlating the instantaneous velocity fluctuations v_i between signals of the two Profilers measured simultaneously. Herein the



(A) Experimental channel



(B) Coordinated sketch of Profiler 1 (left) and Profiler 2 (right)



(C) Detailed sketch of the sampling profiles, looking downstream

Fig. 2. Definition sketch of the experimental facility including the Profilers.

ensemble-averaged experiments were repeated 25 times, and the velocity fluctuation v_i was estimated as $v_i = V_i - \bar{V}_i$, where V_i and \bar{V}_i are respectively the instantaneous and ensemble-averaged median velocity of component i over the 25 repeats. Fig. 3 shows a schematic description of how the calculations were performed between signals of the two sampling volume. For each point (y_n^1, z_n^1) in the sampling profile of Profiler 1 with n ranging from 1 to 35, the velocity fluctuation data v_i were cross-correlated between (y_n^1, z_n^1) and a point (y_n^2, z_n^2) in the sampling profile of Profiler 2 using:

$$R_{yz,i}(\tau) = \frac{\overline{v_{(y_n^1, z_n^1),i}(t)} v_{(y_n^2, z_n^2),i}(t + \tau)}}{\sqrt{\overline{v_{(y_n^1, z_n^1),i}^2} \overline{v_{(y_n^2, z_n^2),i}^2}}} \quad (2)$$

where the overbar denotes an ensemble-average process. In the following section, the approach is applied to all three velocity fluctuation components, and to the tangential Reynolds stress components $v_x v_y$, $v_x v_z$ and $v_y v_z$.

The integral time scale T_{in} may be calculated from the space-time cross-correlation functions between the velocity signals sampled by the two Profilers. The integral time T_{in} is defined as the integral of the cross-correlation functions with respect to the lag in time, between the

Table 1
Experimental flow conditions for ensemble-averaged velocity measurements in a breaking surge using an array of two Profilers (Present study).

Ref.	S_o	Q (m ³ /s)	d_1 (m)	h (m)	z/d ₁ Prof. 1	z/d ₁ Prof. 2	y/B Prof. 1	y/B Prof. 2	U (m/s)	Fr ₁	X location
1a	0	0.101	0.174	0	0.01–0.20	0.17	0.5	0.46–0.51	1.15	1.52	z/d ₁ = 0.17 y/B = 0.50
1b			0.176		0.09–0.28	0.26			1.11	1.50	z/d ₁ = 0.26 y/B = 0.50
1c			0.176		0.23–0.43	0.40			1.18	1.55	z/d ₁ = 0.40 y/B = 0.50

Notes: B: channel width; d_1 : initial water depth recorded at $x = 8.5$ m; Fr₁: compression wave Froude number at $x = 8.5$ m; h: gate opening after closure; Q: initially steady water discharge; U: compression surge celerity positive upstream at $x = 8.5$ m; X: point of intersection of two Profilers' sampling volumes in the y-z plane; y: transverse distance from the right sidewall; z: vertical elevation measured above the bed.

optimum time lag T_i and the first zero of the function after T_i as:

$$T_{in} = \int_{\tau(R_{yz,i}=R_{max})}^{\tau(R_{yz,i}=0)} R_{yz,i}(\tau) d\tau \quad (3)$$

where $R_{yz,i}(\tau)$ is the cross-correlation coefficient of the velocity component i ($i = x, y, z$) calculated between sampling points of Profiler 1 and 2 in a y-z plane. In Eq. (3), T_{in} is positive and the units are seconds, and the first point of the sampling volume was counted as the point located the closest to the ADV emitter. Basically T_{in} represents the longest connection in the turbulent behaviour of the investigated velocity or velocity fluctuation [15,17,10].

In practice, noise issues with Profiler measurements need to be considered when interpreting the space-time cross-correlation data. In the present study, the two sampling profiles of Vectrino II Profilers were intersected about their respective “sweet spots”. The “sweet spots” were locations where the signal quality was the best and corresponded to the one third to one half of the sampling profile, usually the 10th to 20th points [12,38,27,23,13]. While cross-correlation calculations were performed for all points throughout the sampling volume, it is acknowledged that the signals near the two ends of the sampling profiles were of poor quality, and may yield low to zero correlation. Simply, outside the “sweet spots”, the data might not be a true representation of the flow physics.

3.2. Calculations of velocity gradient, strain rate and vorticity

For inhomogeneous turbulence in a spatially and temporally varying turbulent flow, the instantaneous velocity gradient tensor constitutes an important characteristics [26]. The nine simultaneous components of the velocity gradient tensor field at a point in space (x, y, z) at a time t can be expressed as:

$$\frac{\partial V_i}{\partial x_j} = \begin{pmatrix} \partial V_x/\partial x & \partial V_x/\partial y & \partial V_x/\partial z \\ \partial V_y/\partial x & \partial V_y/\partial y & \partial V_y/\partial z \\ \partial V_z/\partial x & \partial V_z/\partial y & \partial V_z/\partial z \end{pmatrix} \quad (4)$$

where V_x is the instantaneous longitudinal velocity component, V_y is the instantaneous transverse velocity component and V_z is the instantaneous vertical velocity component; i and j denote the x, y and z coordinate directions. The vorticity vector at this point and time can thus be determined from the velocity gradient tensor since:

$$\omega_x = \left(\frac{\partial V_z}{\partial y} - \frac{\partial V_y}{\partial z} \right) \quad (5a)$$

$$\omega_y = \left(\frac{\partial V_x}{\partial z} - \frac{\partial V_z}{\partial x} \right) \quad (5b)$$

$$\omega_z = \left(\frac{\partial V_y}{\partial x} - \frac{\partial V_x}{\partial y} \right) \quad (5c)$$

where ω_x, ω_y and ω_z stand for the vorticity component about the x, y and z axes respectively [10]. The three shear components of the strain rate tensor are hence:

$$S_{xy} = \frac{1}{2} \left(\frac{\partial V_x}{\partial y} + \frac{\partial V_y}{\partial x} \right) \quad (6a)$$

$$S_{yz} = \frac{1}{2} \left(\frac{\partial V_y}{\partial z} + \frac{\partial V_z}{\partial y} \right) \quad (6b)$$

$$S_{zx} = \frac{1}{2} \left(\frac{\partial V_z}{\partial x} + \frac{\partial V_x}{\partial z} \right) \quad (6c)$$

The enstrophy $\omega_i\omega_i$, enstrophy production rate $\omega_i S_{ij}\omega_i$, and the

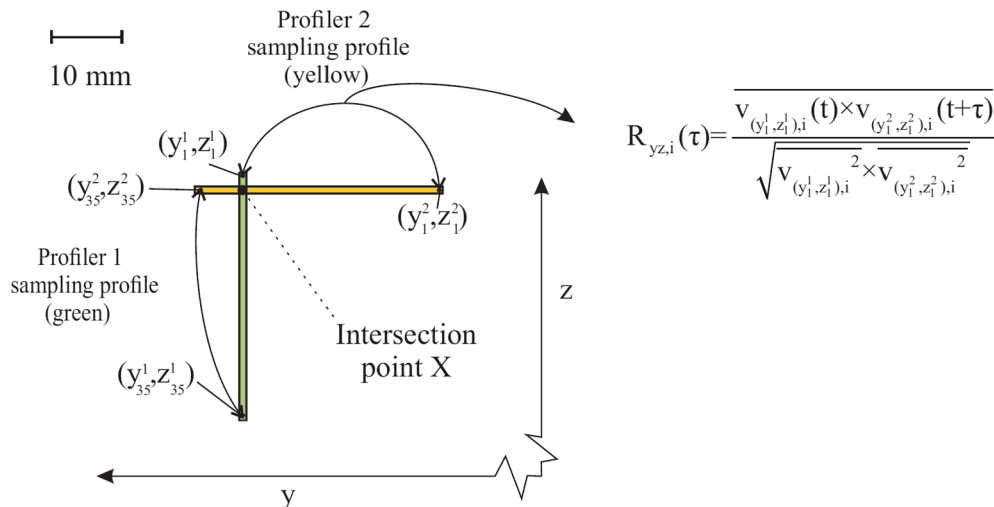


Fig. 3. Cross-correlation calculation between the two sampling profiles of Profiler 1 and 2: a graphical description looking downstream (refer also to Fig. 2C).

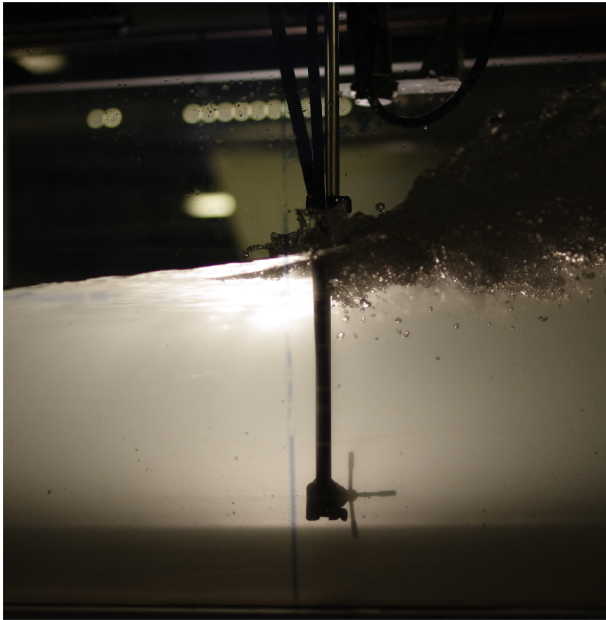


Fig. 4. Breaking bore roller propagation, from right to left, past the Profiler 2 – Shutter speed 1/2000 s with backlighting.

kinetic-energy dissipation rate $2\nu S_{ij}S_{ij}$ may thus be calculated from the above quantities, and used to characterise the small scale turbulence in the open channel shear flows.

In the present study, the velocity gradient tensor $\partial V_y/\partial z$ and $\partial V_z/\partial y$ and its ensemble-averaged time-variations were derived from the Profiler 1 and 2 measurements. The two sampling profiles had one intersection point X for each of the three vertical elevations (Fig. 3). At the point of intersection X, the velocity gradient tensor components $\partial V_y/\partial z$ and $\partial V_z/\partial y$ were both known, and the vorticity about the x-axis ω_x and the shear component of the strain rate tensor S_{yz} were calculated. Table 1 (last column) summarises the y and z coordinates of the point of intersection X.

4. Basic flow observations

Both visual observations, and free-surface elevation and velocity data, showed that the passage of the hydraulic jump in translation was linked to an abrupt rise in water level and longitudinal deceleration (Figs. 4 and 5). Fig. 4 presents a photograph of the breaking bore. Fig. 5 shows dimensionless time-variations of the water depth, longitudinal velocity median V_{median} and longitudinal velocity fluctuations $V_{75}-V_{25}$, where V_{75} and V_{25} are respectively the instantaneous third and first quartiles. Herein the instantaneous velocity fluctuations were calculated as the interquartile range of the ensemble.

The compression wave had a marked roller with some air bubble entrainment, as seen in Fig. 4. The roller was a highly turbulent region with large-scale coherent structures. Most entrained bubbles were contained in the upper roller region, i.e. above the initial water elevation. The velocity measurements showed a rapid flow deceleration with the arrival of the roller. Next to the bed, negative longitudinal velocity was observed at the end of the deceleration (Fig. 5). Such a transient recirculation was recorded for vertical elevations $z/d_1 < 0.3-0.5$. The velocity measurements showed further a large increase in velocity fluctuations during the surge passage, for all velocity components, throughout the entire water column.

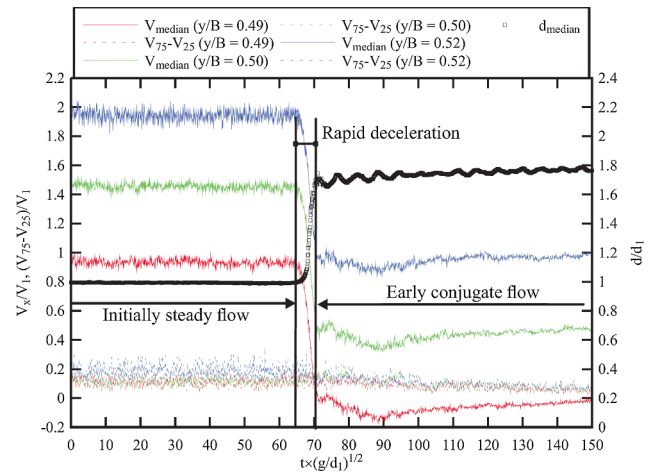


Fig. 5. Ensemble-averaged time-variations of the longitudinal velocity component of a breaking bore, measured by Profiler 2 at $z/d_1 = 0.17$ and $y/B = 0.48-0.53$ – Velocity data offset by +0.5 for each further transverse location with $t = 0$ at Tainter gate closure.

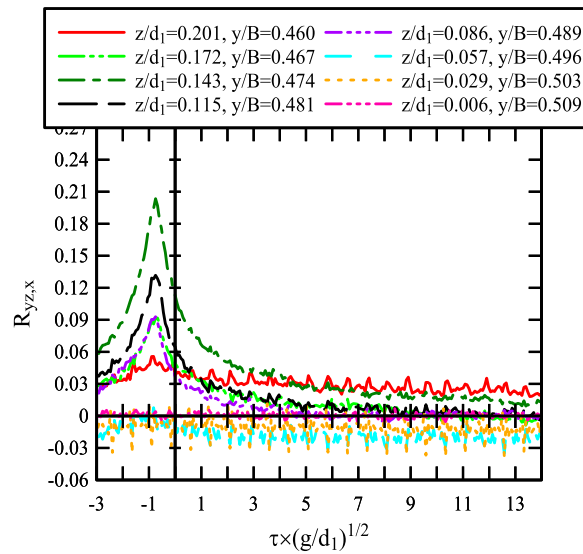
5. Two-dimensional turbulent time and length scales

5.1. Space-time cross-correlations in a two-dimensional plane

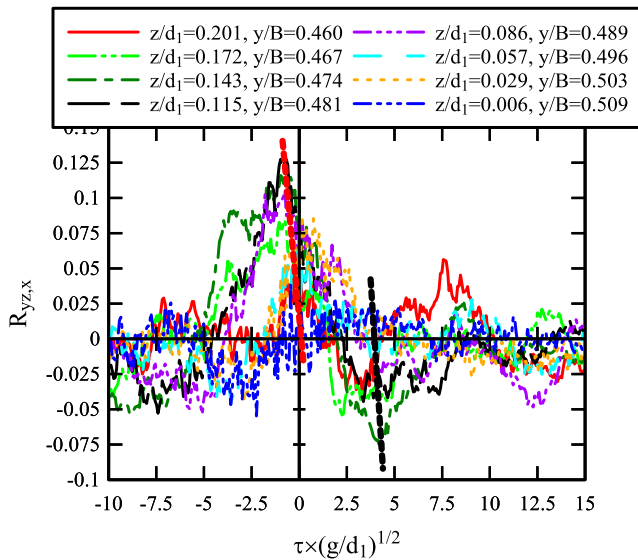
The cross-correlation functions R_{yz} showed bell-shapes at different flow phases of the compression wave. The data sets recorded during the compression wave propagation was divided into three flow phases: (1) the initially steady flow phase, (2) the rapid deceleration phase during which the free-surface rises abruptly, and (3) the early conjugate flow phase where the free-surface changes more gradually with large fluctuations (Fig. 5). The initially steady flow phase was defined as the time from the start of the data collection until the time at which the bore reached the data collection point ($x = 8.5$ m). The rapid deceleration phase took place between the time at which the bore reached the data collection point and the first local minimum reached at the end of the rapid deceleration of longitudinal velocity. The early conjugate flow phase followed immediately after the end of the previous phase i.e. rapid deceleration and ended with the end of the data collection.

For the steady flow period, cross-correlation calculations were performed for 60 s. During the rapid deceleration, the calculations were performed for 1–3 s. The calculation of the conjugate flow phase was performed for 10 s of data, starting from the end of the rapid deceleration phase.

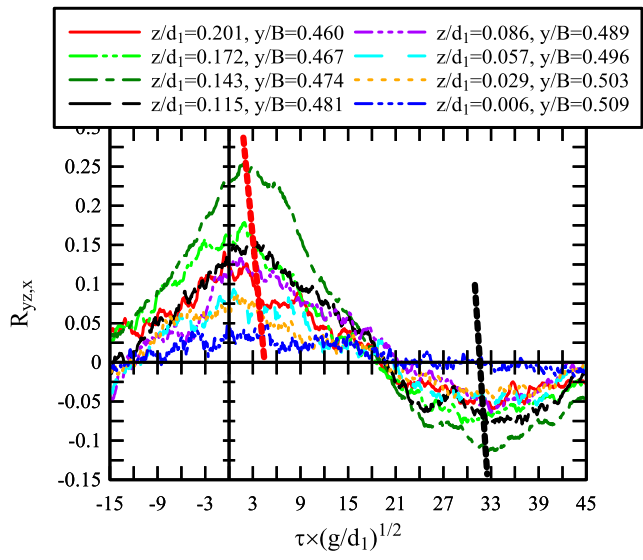
The majority of the data were associated with a maximum cross-correlation coefficient $R_{yz,max}$ at a negative time lag in the initially steady flow (Fig. 6A). Fig. 6 presents typical ensemble-averaged results of the cross-correlation functions $R_{yz,i}$ for the longitudinal velocity. In steady flow, the largest values of $R_{yz,max}$ were observed between the vertical elevations $z/d_1 = 0.10-0.15$ and transverse locations $y/B = 0.47-0.48$, which was approximately at the first one third of the two sampling volumes (the first one third represents the 10th–12th points out of the total 35 points in the sampling profile), corresponding to the “sweet spots” of the sampling profiles. The position of the maximum value of $R_{yz,max}$ was not at the point X where the two sampling volumes intersected, i.e. $z/d_1 = 0.172$, $y/B = 0.5$, but slightly lower in terms of vertical elevation, and more towards the right sidewall. The maxima in cross-correlation functions increased first as the y- and z-coordinates increased, then decreased with increasing y- and z-coordinate, after the peak value was reached at $z/d_1 = 0.10-0.15$ and $y/B = 0.47-0.48$. Away from both emitters ($z/d_1 < 0.06$ and $y/B > 0.50$), the correlations between the two Profiler signals were weak and barely showed any marked peaks. Compared to single Profiler measurements, the cross-correlations between the two probes were in



(A) Steady



(B) Rapid deceleration



(C) Conjugate flow

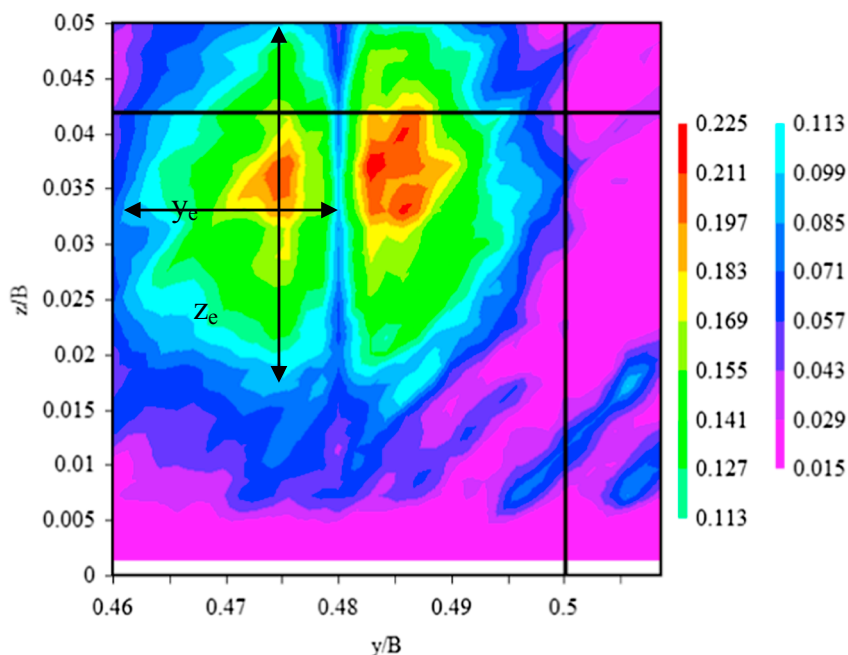
Fig. 6. Cross-correlation functions between velocity signals of two Profilers in the longitudinal direction during the steady flow, rapid deceleration and conjugate flow phases for a compression wave – Flow conditions: $Q = 0.101 \text{ m}^3/\text{s}$, $d_1 = 0.174 \text{ m}$, $Fr_1 = 1.52$, $x = 8.5 \text{ m}$, $y/B = 0.46\text{--}0.51$, $z/d_1 = 0.00\text{--}0.20$.

general weaker, with the peak coefficient being an order of magnitude smaller.

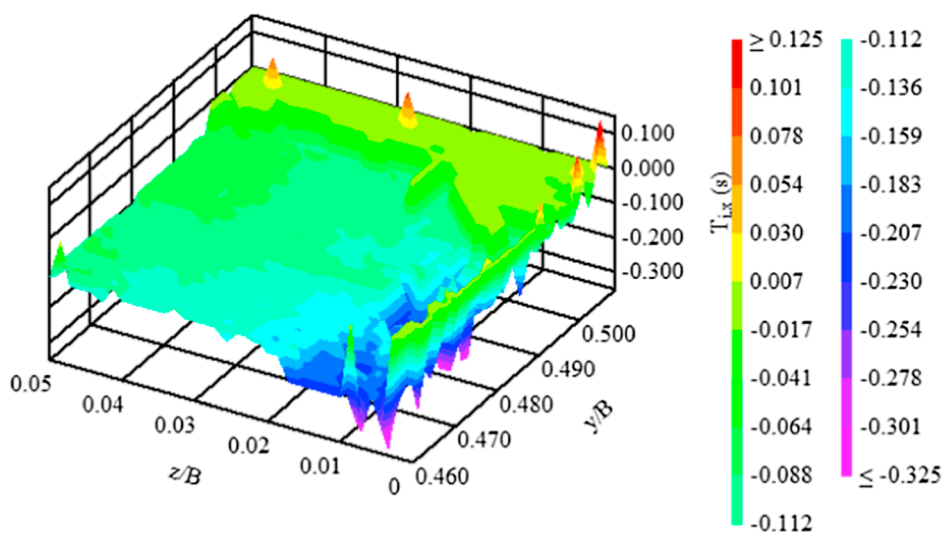
During the rapid deceleration and conjugate flow phases, all cross-correlation functions showed a double-peak pattern, marked by the red dashed line and by the black dashed line in Fig. 6B and C. One peak corresponded to a positive peak in cross-correlation, while the other often presented a negative cross-correlation. The two peaks were associated with a negative and positive time lag for the rapidly-varied flow phase, while both peaks were linked to positive time lags for the conjugate flow phase. During the rapid deceleration, the peaks showed comparable magnitudes, although one peak was always negative. During the conjugate flow phase, the positive peaks were mostly associated with larger magnitudes, compared to the negative peaks. For all three phases, maximum values of peak coefficient $R_{yz,max}$ were found at $z/d_1 = 0.10\text{--}0.15$ and $y/B = 0.47\text{--}0.48$, i.e. at the first third of the two sampling profiles. For higher vertical elevations ($0.20 < z/d_1 < 0.43$), the positions of the maximum peak cross-correlation were consistent with observations at lower vertical elevations (at the first

third of the two sampling profiles).

The contours of maximum cross-correlation coefficients R_{max} were calculated, where R_{max} is the maximum of $R_{yz,i}$ at an optimum time lag T_i on the plane formed by the two orthogonal velocity profiles. Typical results were shown in Fig. 7 for the longitudinal velocity component during three different flow phases of compression wave propagation. The horizontal and vertical axes are respectively the absolute transverse and vertical coordinates, with the transverse coordinate $y = 0$ at the right sidewall and the vertical coordinate $z = 0$ at the channel bed. During the steady flow phase, the results highlighted two large coherent structures formed towards the upper left corner of the sampling plane. The approximate transverse and vertical length scales of each structure, denoted respectively y_e and z_e , are defined in Fig. 7A (A.1). The size of the coherent structures corresponded to a maximum transverse length scale of $y_e/B = 0.015$ ($y_e/d_1 = 0.06$) and maximum vertical length scale of $z_e/B = 0.035$ ($z_e/d_1 = 0.14$), where B is the channel width ($B = 0.7 \text{ m}$) and d_1 is the initially steady flow depth ($d_1 = 0.174 \text{ m}$). A similar pair of coherent structures was found in the iso-correlation



(A.1) Steady flow: maximum cross-correlation coefficients R_{max}



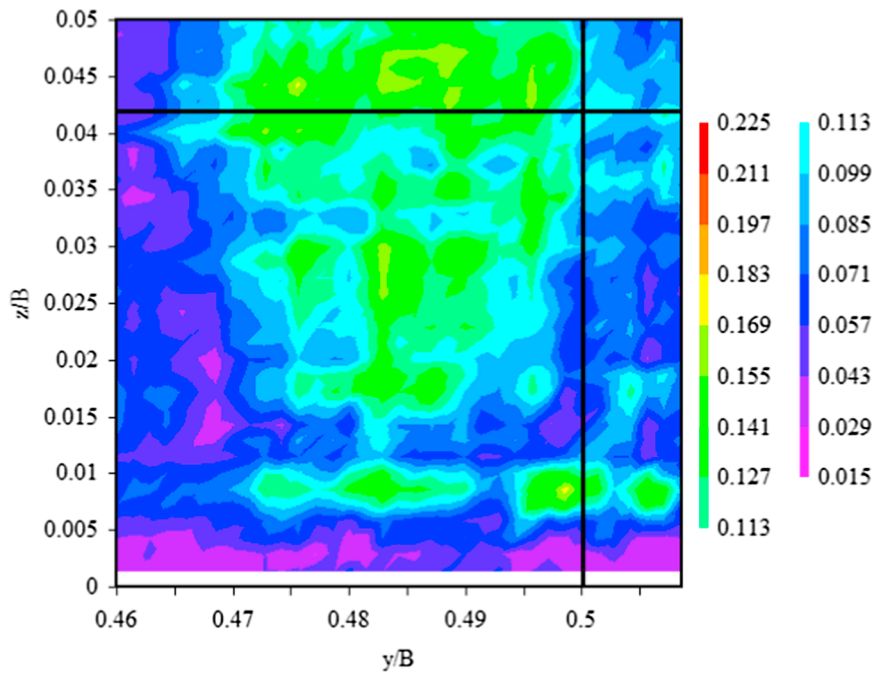
(A.2) Steady flow: optimum time lag T_i

Fig. 7. Contours of maximum cross-correlation coefficients R_{max} and optimum time lag T_i between the longitudinal velocity components sampled by the two Profilers during the three flow phases of bore propagation; black solid lines denote location of the two sampling profiles - Flow conditions: $Q = 0.101 \text{ m}^3/\text{s}$, $d_1 = 0.174 \text{ m}$, $Fr_1 = 1.52$, $z/d_1 = 0.00\text{--}0.20$, $y/B = 0.46\text{--}0.51$.

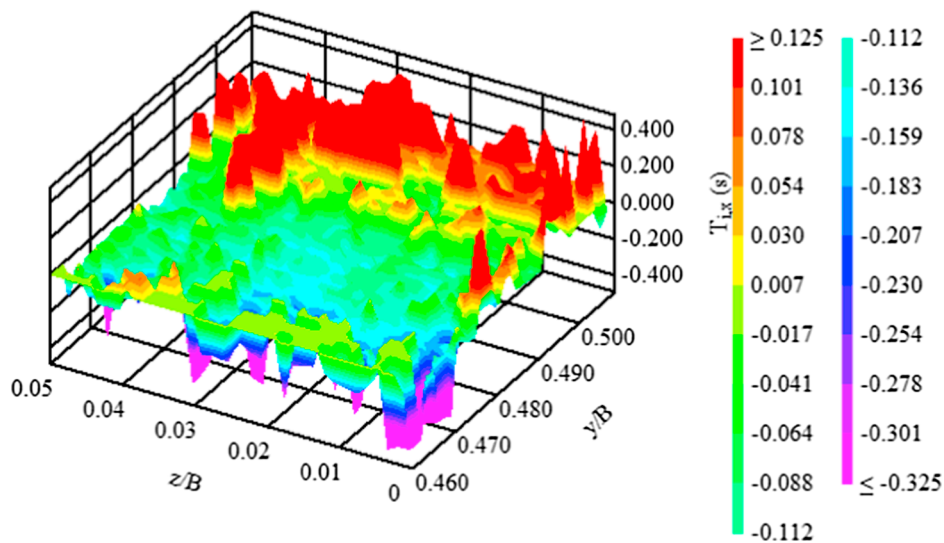
contours, calculated from the transverse and vertical velocity components, suggesting that the structures were three dimensional. The coherent structures, highlighted by iso-correlation contours of transverse velocity components, showed more elongation in the transverse direction whereas the structures from the vertical velocity correlations showed more elongation in the vertical direction. The flow coherence could be linked to some “hairpin” vortex, formed in turbulent boundary flow near the bottom boundary [34,28,37]. Direct numerical simulation of steady flows at low Reynolds number showed the y-z cross-sectional view of the hairpin vortex being very similar to the shape highlighted in

Fig. 7 [39]. The coherent turbulent structures observed in the present study showed similar dimensionless size compared to previous numerical studies [2,37].

The optimum time lags T_i corresponding to the iso-correlation contours of the maximum space-time correlation coefficients are presented in Fig. 7(A.2, B.2, C.2). Viewed in three-dimensions, the optimum time lag T_i in the initially steady flow showed an increase from negative to positive lags with increasing transverse and vertical directions. It was noted that, near the bottom and right boundary of the sampling plane ($z/B < 0.015$ and $y/B > 0.51$), the maximum cross-



(B.1) Rapid deceleration: maximum cross-correlation coefficients R_{\max}



(B.2) Rapid deceleration: optimum time lag T_i

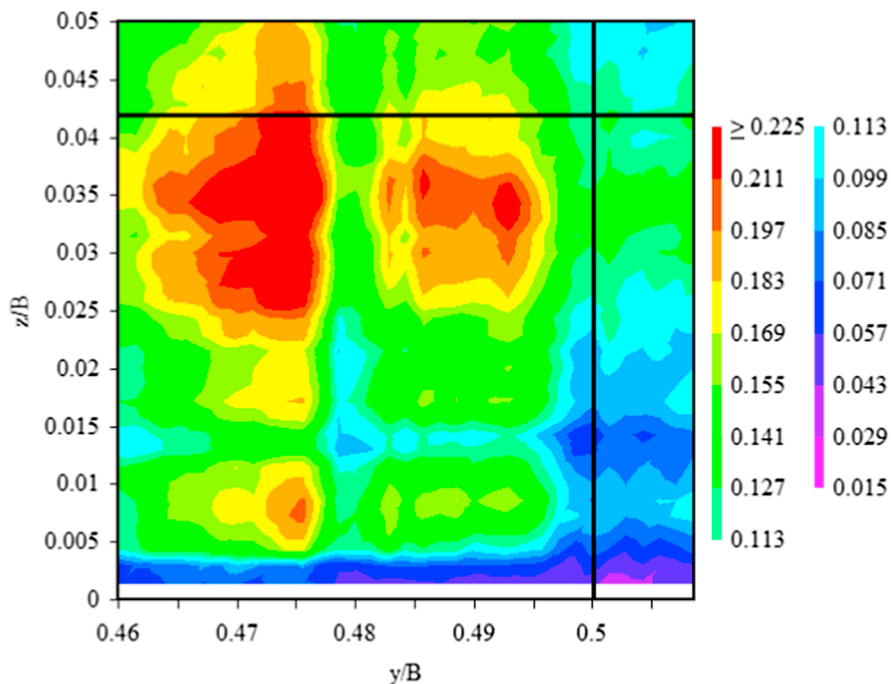
Fig. 7. (continued)

correlation coefficients R_{\max} were smaller than 0.02, and the optimum time lag might not be physically meaningful. Nevertheless, the optimum time lags highlighted organised motions of turbulence next to the channel bed in the steady open channel flows. Within the sampled y - z plane and during the initially steady flow, coherent structures were formed near the right side wall, and moved up in the vertical direction towards the channel centreline.

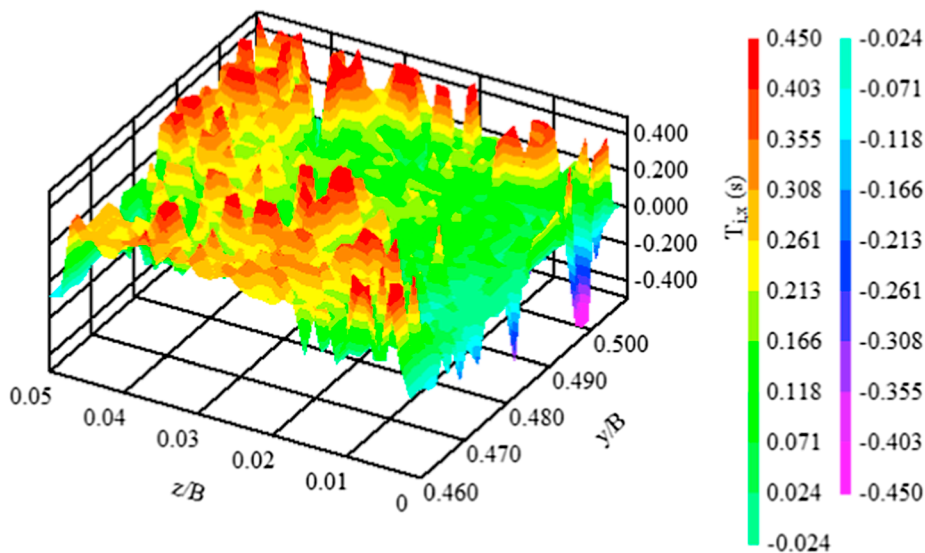
During the rapid deceleration phase corresponding to the compression wave passage, the magnitudes of R_{\max} decreased throughout the sampled plane. The iso-correlation contour lines expanded and seemingly merged into one large scale coherent structure. The maximum width of the structure was $y_e/B \sim 0.05$ ($y_e/d_1 \sim 0.20$) and the maximum height was $z_e/B \sim 0.046$ ($z_e/d_1 \sim 0.19$) (Fig. 7A.1). The optimum time lags, on the other hand, showed an overall increase in

positive values during the two highly unsteady flow phases (Fig. 7B.2 & C.2). Compared to the initially steady flow phase, the optimum time lags during the rapid deceleration phase showed quasi-homogeneity in the vertical direction. It consistently increased with increasing transverse coordinates for all vertical elevations. The time lags decreased from positive to negative with distance away from the channel centreline, indicating organised turbulent motions from the right side wall towards the channel centreline during the rapid deceleration phase, encompassing the entire vertical sampling frame.

During the conjugate flow phase following the rapid deceleration phase, the single large-scale structure broke up into two coherent structures, the dimensions of which were much larger compared the steady flow phase. The boundary of the iso-correlation lines at the edge of these coherent structures was out of the sampling frame (Fig. 7C.1).



(C.1) Conjugate flow: maximum cross-correlation coefficients R_{max}



(C.2) Conjugate flow: optimum time lag T_i

Fig. 7. (continued)

The vertical size of the coherent structures was $z_e/B \sim 0.05$ ($z_e/d_1 \sim 0.20$) and the maximum width of each pocket was at least $y_e/B \sim 0.02$ ($y_e/d_1 \geq 0.080$). During the conjugate flow phase, the optimum time lags showed positive values near the left and right edges of the sampling plane ($y/B \sim 0.46$ and $y/B \sim 0.51$), and slightly negative values in the middle of the sampled plane. The results highlighted turbulent motions initiated in the middle of the sampling frame and moving in the two opposite directions of the transverse axis.

Table 2 summarises the transverse and vertical length scales of the coherent structures, for the three velocity components V_x , V_y and V_z during each different flow phase. During the rapid deceleration flow phase, the coherent structures found in the transverse and vertical velocity components broke up and were associated with no clear boundaries, hence the “N/A” input. During the conjugate flow phase, the

structure in the vertical velocity direction was not well defined either. Despite being indefinite in some flow phases, the coherent structure projected in the y - z plane expanded in the longitudinal velocity component as the bore passed. For the transverse velocity component, the structure was transversely stretched after the bore passage in the conjugate flow phase.

At the highest range of vertical elevations ($z/d_1 = 0.23$ – 0.43), the results showed some notable difference compared to the lowest range of vertical elevations. Fig. 8 shows iso-correlation contours of R_{max} measured in a y - z plane with $y/B = 0.46$ – 0.51 and $z/d_1 = 0.23$ – 0.43 during the initially steady flow. For all velocity components, the results highlighted two seemingly isolated coherent structures, one spanned a lower vertical range ($z/d_1 = 0.26$ – 0.40) and one, apparently initiated and detached from the lower structure, spanning a higher vertical range

Table 2

Transverse and vertical length scales y_e and z_e of coherent structures highlighted by iso-correlation contours of the maximum cross-correlation coefficient R_{\max} for three velocity components during different flow phases.

S_o	Q (m^3/s)	d_1 (m)	h (m)	Fr_1	X location	Velocity component	Steady		Rapid deceleration		Conjugate flow	
							y_e/B	z_e/B	y_e/B	z_e/B	y_e/B	z_e/B
0	0.101	0.174	0	1.52	$z/d_1 = 0.17$ $y/B = 0.50$	Longitudinal (V_x)	0.02	0.04	0.05	0.05	0.02	0.05
						Transverse (V_y)	0.02	0.02	N/A	N/A	0.02	0.01
						Vertical (V_z)	0.01	0.03	N/A	N/A	N/A	N/A

Notes: X is the point of intersection of two Profilers' sampling volumes in the y - z plane; The two sampling volumes were separated by a longitudinal distance of 0.075 m; N/A denotes the absence of detectable large-scale coherent structure in the y - z plane.

($z/d_1 = 0.4$ – 0.425). The lower structure ($z/d_1 < 0.25$), as shown in Fig. 8B, could correspond to some structure observed at lower vertical elevations (as in Fig. 7). The upper structure showed various shapes and sizes for different velocity components, and differed slightly from the structure observed at lower vertical elevations. Overall, the upper coherent structure appeared to be vertically elongated with space-time cross-correlations of the transverse velocity component, and transversely elongated with space-time cross correlations of the vertical velocity component. The results suggested that, at a higher vertical elevation, turbulent structures were formed probably by detachment from coherent structures generated near the bed, then evolving in a three-dimensional manner. The length scale of the width and height of the detached turbulent structure were comparable to the one formed near the bed. The difference in terms of transverse and vertical dimensions from different velocity components could be linked to the shearing of the fluid at such locations, resulting in the structure to distort and rotate in response to the shear stresses.

The space-time cross-correlations of the instantaneous tangential Reynolds stress components $v_x v_y$, $v_x v_z$ and $v_y v_z$ were further calculated. Full details are reported in Leng and Chanson [24]. The maximum cross-correlation coefficients of ensemble-median cross-correlation functions throughout the plane were drastically smaller, compared to results from the velocity fluctuations. Out of the three tangential stresses, only the $v_y v_z$ component exhibited a distinctively marked peak in terms of the cross-correlation functions, with a maximum about one order of magnitude lower than velocity component results. Such a finding was deemed reasonable considering that the cross-correlation calculations were performed across the y - z plane, and hence the shear stress component $v_y v_z$ would be expected to play a predominant role. Typical iso-correlation contours of the maximum cross-correlation coefficients calculated from the instantaneous stress component $v_y v_z$ are presented in Fig. 9, for the highest range of vertical elevations within the experimental flow conditions. The iso-correlation contours of $v_y v_z$ showed two crests in R_{\max} (highlighted by dashed circles), corresponding to the two positions where the centre of coherent structures were observed in Fig. 8B and C. These crests were associated with large values of R_{\max} , which could represent two peaks of localised shear stress. This could explain the shape of the iso-correlation contours of the transverse and vertical velocity components, where the effect of localised tangential stress $v_y v_z$ resulted in stretches of coherent structures in the respective transverse and vertical directions.

5.2. Integral and turbulent scales in the two-dimensional y - z plane

The integral time T_{in} may be calculated from the space-time cross-correlation functions between the velocity signals sampled by the two Profilers (Eq. (3)). T_{in} represents the longest connection in the turbulent behaviour of the investigated velocity or velocity fluctuation, also referred to as the “memory time” of the turbulent flow [15,17,10]. Typical results in the initially steady flow are shown in Fig. 10 for all velocity components. In Fig. 10, the contour values stand for the magnitudes of T_{in} in seconds throughout the investigated y - z plane. Note that the T_{in} data were post-processed to remove spurious data

when the associated R_{\max} was small and not meaningful (e.g. $R_{\max} < 0.1$) or the optimum time lag was too large (e.g. $T_i > 0.1$ s). Overall the “memory time” T_{in} ranged from 0 to 0.05 s for all flow phases. Similarities may be found with the iso-correlation contours of the respective velocity components (Fig. 7), where areas of significant T_{in} values coincided with areas of large cross-correlation coefficients of velocity fluctuations. The magnitudes of T_{in} were overall higher for the longitudinal velocity component, i.e. maximum $T_{in} < 0.05$ s, and lower for the transverse velocity component, i.e. maximum $T_{in} < 0.03$ s. The results indicated that the flow before the compression wave was three-dimensional, anisotropic, and possibly associated with a longer coherence in the longitudinal direction compared to the other two flow directions.

During the following two flow phases, i.e. the rapid deceleration flow phase and the conjugate flow phase, the integral time T_{in} showed some drastic changes. Fig. 11 illustrates typical results for the longitudinal velocity component. The results were very consistent for the other two velocity components. During the rapid deceleration, the magnitudes and total area for $T_{in} > 0.01$ s remained similar to those for the steady flow phase, but the position of the contour line $T_{in} = 0.01$ s shifted slightly towards the channel centreline. During the conjugate flow phase, the values of T_{in} were overall one order of magnitude higher, i.e. from 10^{-2} s to 10^{-1} s. The area of regions with high T_{in} ($T_{in} > 0.01$ s) also expanded significantly in terms of both transverse and vertical dimensions. The changes in “memory time” T_{in} during different flow phases of a bore propagation followed the same trend with the evolution of the coherent structures, as found in iso-correlation contours of maximum cross-correlations of velocity fluctuations.

Altogether, the R_{\max} , T_i and T_{in} data seemed to suggest that (1) some large coherent structures were formed within the sampled y - z plane; (2) these structures were three-dimensional and anisotropic; (3) the size of these coherent structures expanded during and after the bore passage; and (4) the motion of the bore passage focalised the structures towards the channel centreline within the sampled y - z plane.

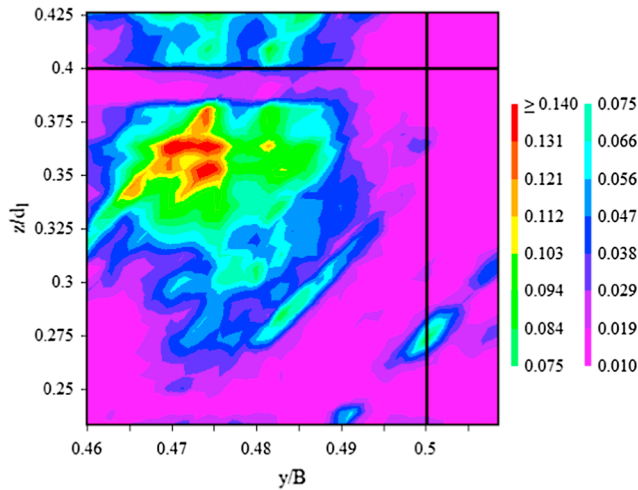
The turbulent integral area of a large scale coherent structure in the y - z plane may be deduced from the maximum cross-correlation coefficient R_{\max} as:

$$A = \int_0^{\Delta z_{\max}} \int_0^{\Delta y_{\max}} R_{\max} dz dy \quad (7)$$

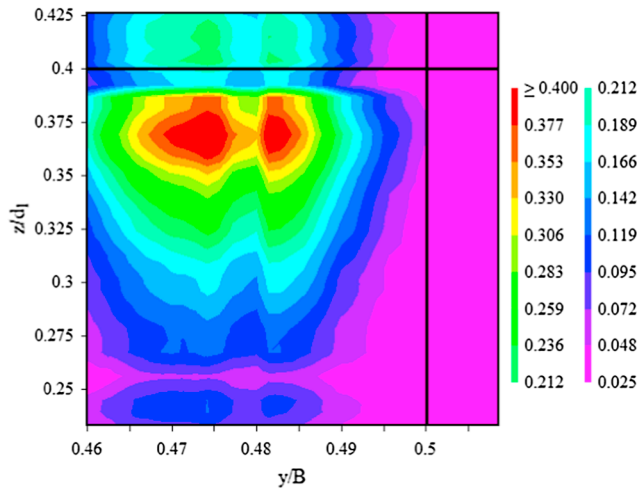
where Δz_{\max} and Δy_{\max} are respectively the maximum vertical and transverse separation distance equal to 0.034 m herein for both directions. The maximum cross-correlation coefficient R_{\max} is a surface function in the y - z plane. A threshold $R_{\max} > 0.1$ was applied herein to filter out signals with negligible correlations. Further, the associated turbulent time scale of such structure was estimated as:

$$T = \frac{1}{A} \int_0^{\Delta z_{\max}} \int_0^{\Delta y_{\max}} R_{\max} T_{in} dz dy \quad (8)$$

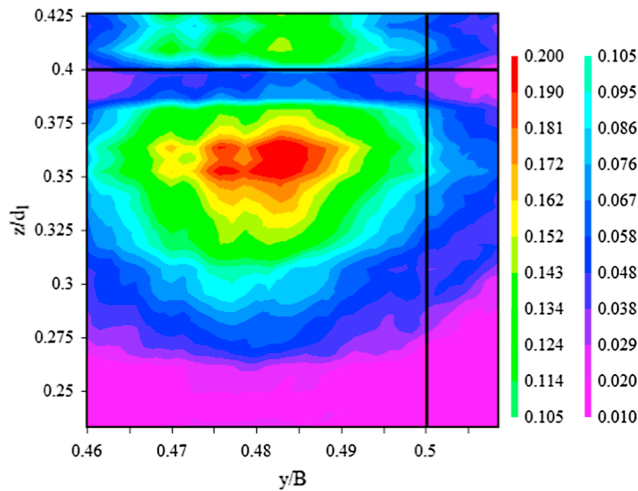
where T_{in} is the optimum time lag associated with R_{\max} where it satisfies $R_{\max} > 0.1$, and A is the area scale. Appendix I summarises the results of the present study. The area scale $A_{y,z,i}$ and time scale $T_{y,z,i}$ in the y - z plane are calculated respective for the three velocity



(A) Longitudinal velocity component



(B) Transverse velocity component



(C) Vertical velocity component

Fig. 8. Contours of maximum cross-correlation coefficients R_{max} calculated from the longitudinal, transverse and vertical velocity components sampled by the two Profilers during the initially steady flow; black solid lines denote location of the two sampling profiles – Flow conditions: $Q = 0.101 \text{ m}^3/\text{s}$, $d_1 = 0.176 \text{ m}$, $Fr_1 = 1.52$, $z/d_1 = 0.23\text{--}0.43$, $y/B = 0.46\text{--}0.51$.

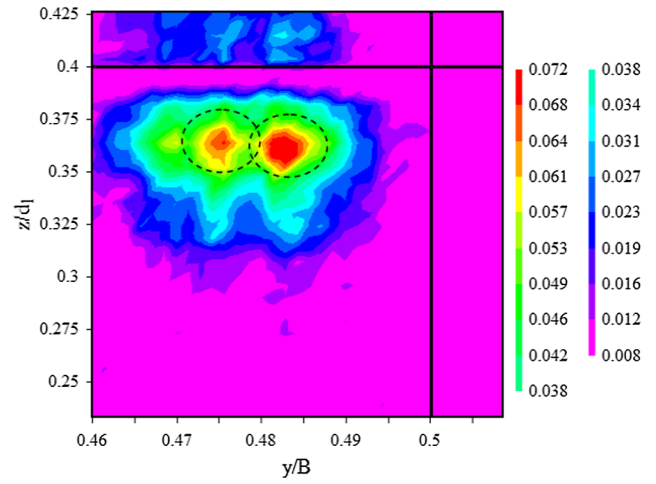
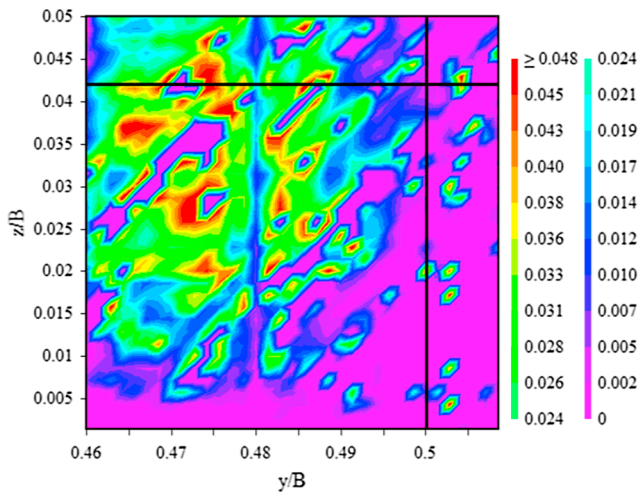


Fig. 9. Contours of maximum cross-correlation coefficients R_{max} calculated from the instantaneous tangential Reynolds stress component $v_y v_z$ sampled by the two Profilers during the initially steady flow; black solid lines denote location of the two sampling profiles – Flow conditions: $Q = 0.101 \text{ m}^3/\text{s}$, $d_1 = 0.176 \text{ m}$, $Fr_1 = 1.52$, $z/d_1 = 0.23\text{--}0.43$, $y/B = 0.46\text{--}0.51$.

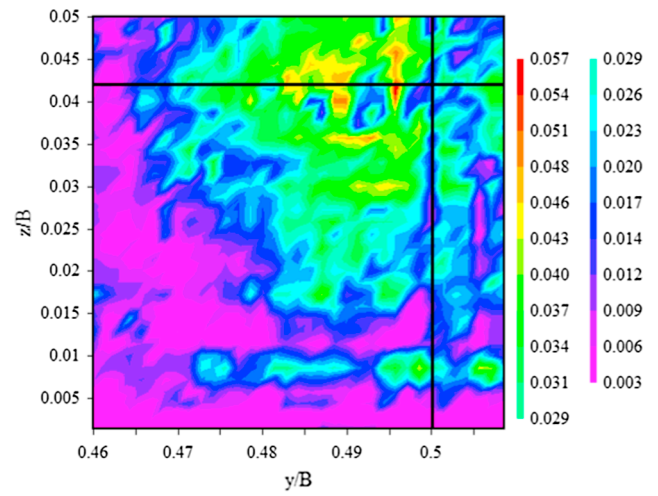
components V_i with $i = x, y, z$ and for the three flow phases associated with compression wave propagations.

The turbulent area scale of a coherent turbulent structure in the $y\text{-}z$ plane showed a variety of magnitudes for the longitudinal, transverse and vertical velocity components during the initially steady flow, ranging from 4 mm^2 to 230 mm^2 . The area scale for the transverse velocity component seemed to be consistently larger than the area scales for the other two velocity components in the steady flow phase, with $A_{yz,y}/A_{yz,x} \sim 2\text{--}28$ and $A_{yz,y}/A_{yz,z} \sim 2\text{--}4$. The surface area time scale in the steady flow ranged from 0.007 s to 0.210 s for all velocity components. At different vertical elevations, the integral area and time scales showed some variation. The area scale for the longitudinal velocity component decreased with increasing vertical elevations. The integral area scales in the y and z -velocity components only fluctuated $\pm 10\text{--}20\%$, as the vertical elevation increased. The time scale for the longitudinal and transverse velocity components showed a common trend, decreasing with increasing vertical elevation, whereas for the vertical velocity component, it varied with no obvious trend. During the rapidly-varied flow phase, the maximum cross-correlation coefficient R_{max} throughout the $y\text{-}z$ sampling plane decreased generally, with the integral area scale in some velocity component decreasing down to zero, when the R_{max} data were all less than 0.1, e.g. $A_{yz,z}$ and $T_{yz,z} = 0$ in Appendix I. For data with large correlation, the area scale increased as the flow phase changed from steady to rapidly-varied, e.g. $A_{yz,x}$ in rapid deceleration/ $A_{yz,x}$ in steady flow = 1.1–14. The surface area time scale data showed little difference between the rapid deceleration and steady flow phases.

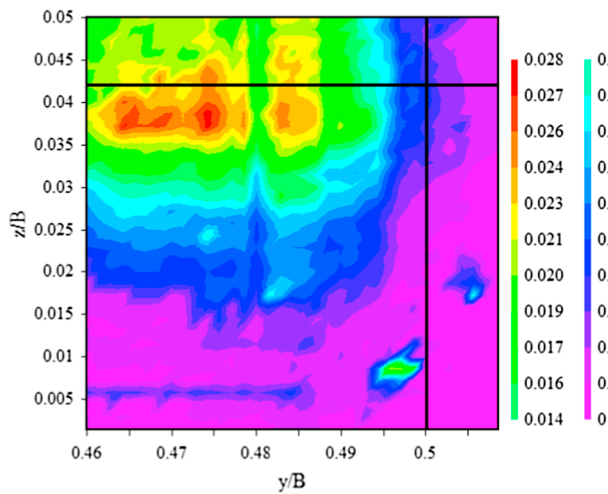
During the conjugate flow phase, both the area and time scale were associated with drastic increases for all velocity components at all vertical elevations, despite a few suspicious data highlighted in *italic font* (Appendix I). For the longitudinal velocity component, the integral area scale was 27 times larger than during the steady flow, whereas the integral time scale was 10 times longer than that in the steady flow, for the transverse velocity component. The results showed some qualitative similarity to the one-dimensional (1D) turbulent time and length scales, calculated respectively for the y and z coordinates (Fig. 12). Fig. 12 presents a comparison between the dimensionless turbulent scales calculated in the 1D and 2D data, where $L_{yy,i}$ is the turbulent integral length scale representing a characteristic transverse size of large coherent structure found in the velocity component i (with $i = x, y$ or z), $L_{zz,i}$ is the turbulent integral length scale representing a characteristic vertical size of large coherent structure found in the velocity direction i , $T_{yy,i}$ is the turbulent integral time scale characterising the time scale or



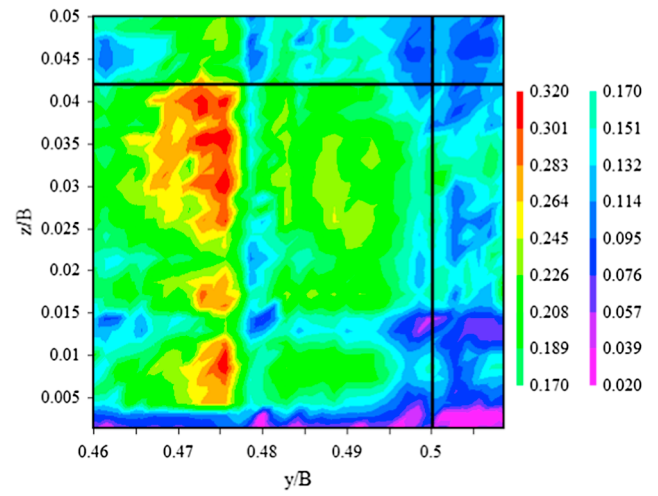
(A) Longitudinal velocity component



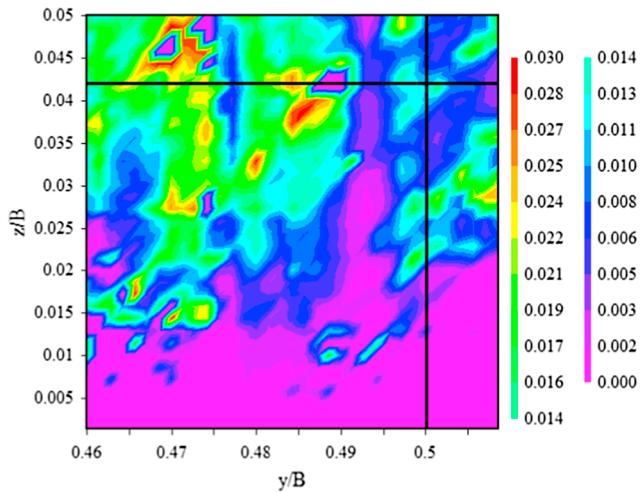
(A) Rapid deceleration



(B) Transverse velocity component



(B) Conjugate flow



(C) Vertical velocity component

Fig. 10. Contours of the integral time T_{in} (s) of the space time cross-correlation functions of the longitudinal, transverse and vertical velocity components sampled by the two Profilers during the initially steady flow - Flow conditions: $Q = 0.101 \text{ m}^3/\text{s}$, $d_1 = 0.174 \text{ m}$, $Fr_1 = 1.52$, $z/d_1 = 0.00-0.20$, $y/B = 0.46-0.51$.

Fig. 11. Contours of the integral time T_{in} (s) of the space time cross-correlation functions of the longitudinal velocity component sampled by the two Profilers during the rapidly-varied flow and conjugate flow phases; flow conditions: $Q = 0.101 \text{ m}^3/\text{s}$, $d_1 = 0.174 \text{ m}$, $Fr_1 = 1.52$, $z/d_1 = 0.00-0.20$, $y/B = 0.46-0.51$.

lifespan of large coherent structure found in the velocity direction i in the transverse direction, and $T_{zz,i}$ is the turbulent integral time scale characterising the time scale of large vortices found in the velocity direction i in the vertical direction. The 2D dimensionless area scales were of the same order of magnitudes as the product of the 1D dimensionless length scales in the respective y and z directions. During the steady flow phase (Fig. 12A), the length and area scales showed consistent trends, decreasing with increasing vertical elevation. As the compression wave propagated, the length and area scales became larger during the rapidly varied flow phase, becoming the largest during the conjugate flow phase. The time scales, on the other hand, showed similar and consistent dimensionless values regardless of the 1D or 2D nature. The time scales, both 1D and 2D, were larger during the conjugate flow phase, and lower during rapidly varied flow phase, with the steady flow phase showing medium values. Overall, the 2D turbulent area and time scales confirmed that the propagation of compression waves is a highly unsteady turbulent process, with large coherent anisotropic turbulent structures formed beneath and behind the bore front.

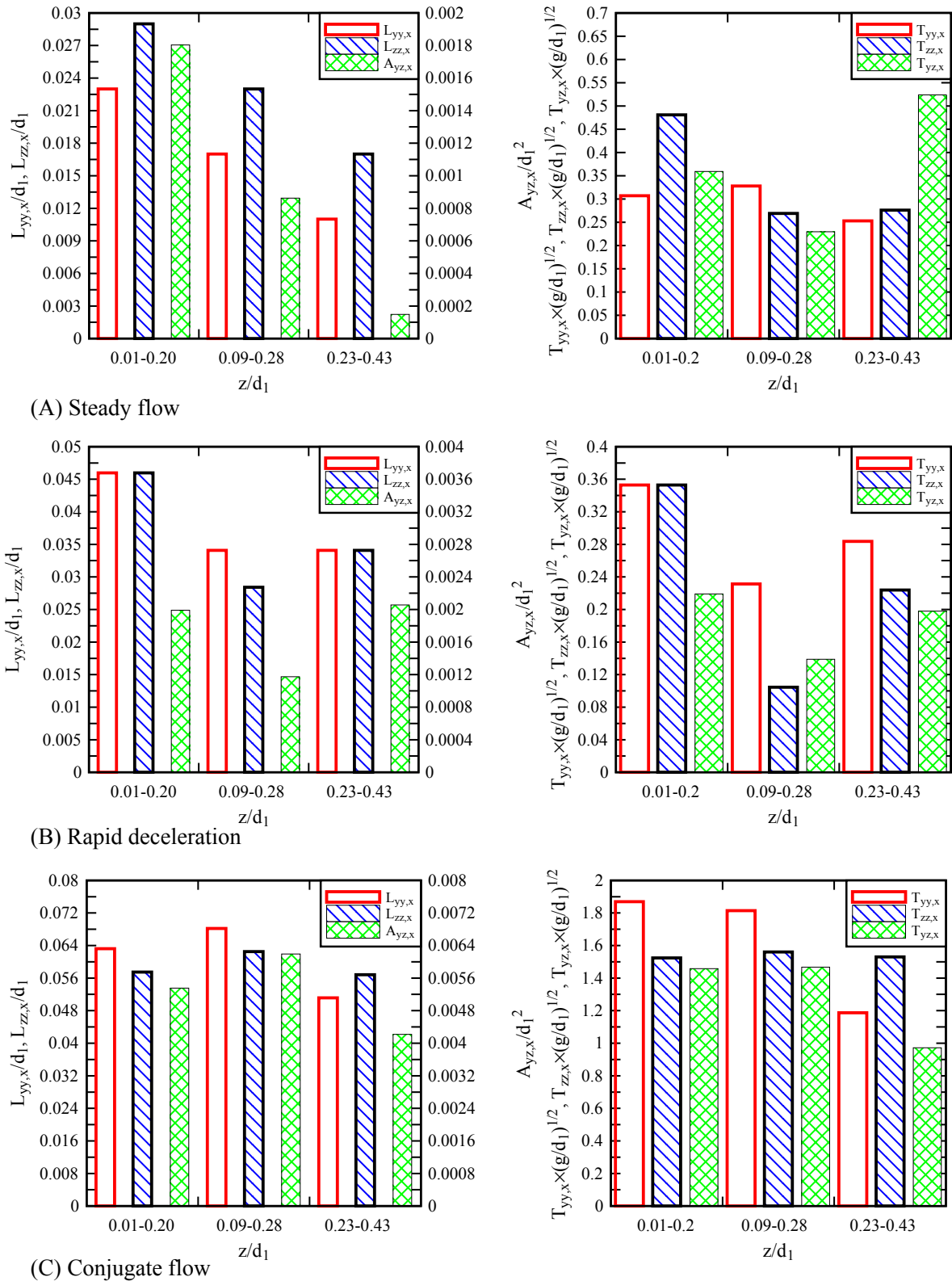


Fig. 12. Comparison of the dimensionless turbulent length (area) and time scales measured in the one-dimensional transverse y, vertical z directions and the two-dimensional y-z plane – Data calculated from the longitudinal velocity component for different flow phases.

6. Velocity gradient tensor, strain rate tensor and vorticity

6.1. Ensemble-averaged velocity gradient and fluctuations

Studies of direct numerical simulations in incompressible,

homogeneous and inhomogeneous turbulence indicate that, in regions of high kinetic energy dissipation rate, the geometry of the local velocity gradient field has a universal character [6].

The ensemble-averaged variations of velocity gradient tensor $\partial V_y/\partial z$ with respect of time and vertical elevation z are presented in Fig. 13.

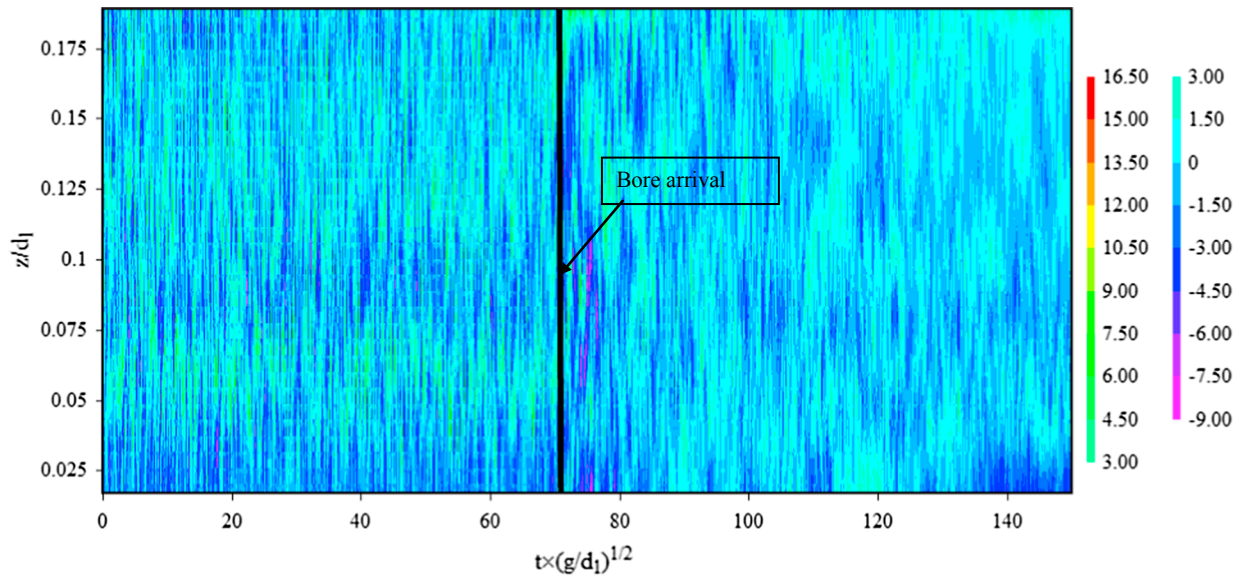
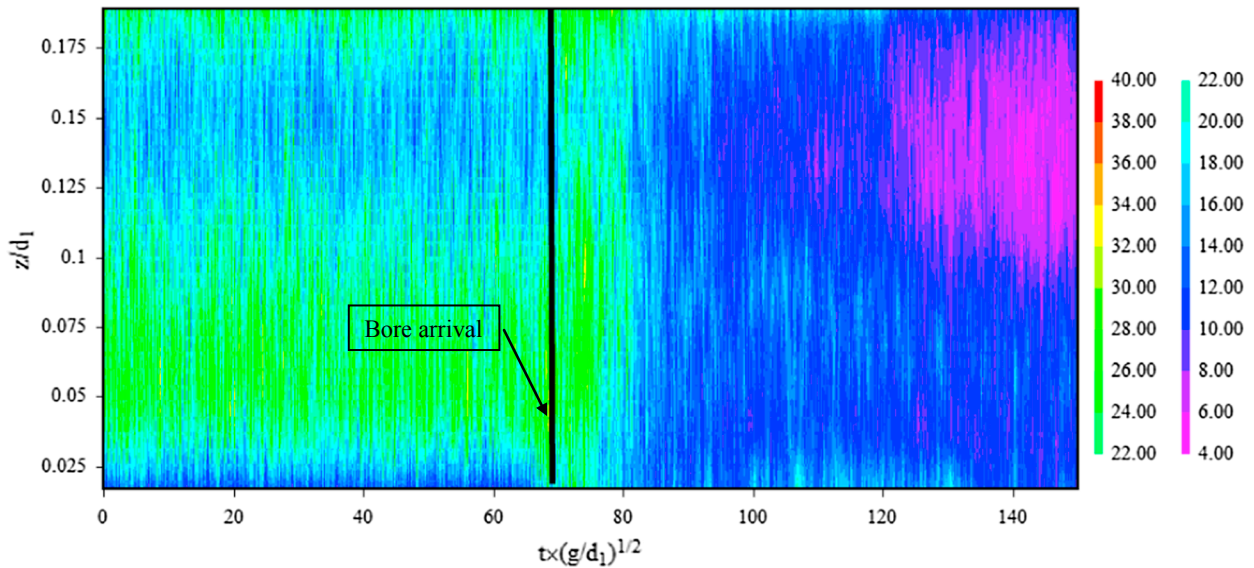
(A) Space-time contour of the ensemble-averaged velocity gradient tensor $\partial V_y/\partial z$ (s^{-1})(B) Space-time contour of the velocity gradient fluctuation of tensor component $\partial V_y/\partial z$ (s^{-1})

Fig. 13. Space-time contour of ensemble-averaged velocity gradient and velocity gradient fluctuations of tensor component $\partial V_y/\partial z$ during the propagation of breaking bores – Flow conditions: $Q = 0.101 \text{ m}^3/\text{s}$, $d_1 = 0.174 \text{ m}$, $Fr_1 = 1.52$, $z/d_1 = 0.00\text{--}0.20$, $y/B = 0.46\text{--}0.51$.

The dimensionless time $t(g/d_1)^{1/2} = 0$ corresponds to the Tainter gate closure, and the bore arrival time at the velocity sampling location is highlighted by the arrow and thick black line. The initially steady flow was observed from $t(g/d_1)^{1/2} = 0$ to the bore arrival time. The velocity gradient tensor $\partial V_y/\partial z$ showed a meandering pattern throughout time and space i.e. the vertical dimension z , with one band corresponding to a negative gradient (dark blue colour) and one band corresponding to a positive gradient (light green colour) (Fig. 13A). The two bands appeared alternatively in the vertical dimension and were associated with rapid fluctuations in the dimension of time. The dimensionless period of these large fluctuations was roughly $T(g/d_1)^{1/2} \sim 10$, corresponding to a period of $T \sim 1 \text{ s}$ in dimensional form.

With the arrival of the bore, the free-surface rose up abruptly and the flow decelerated rapidly at all vertical elevations on the sampling profile. The rapid deceleration phase took approximately 1.3 s, corresponding to a dimensionless duration $\Delta t(g/d_1)^{1/2} \sim 10$. During the

rapid deceleration, the velocity gradient tensor $\partial V_y/\partial z$ showed some drastic fluctuations in both time and space. Immediately after the rapid deceleration, the flow was unsteady and relatively gradually-varied, and the velocity gradient magnitudes were significantly smaller, compared to the initial steady flow phase. A large portion of the vertical profile was associated with zero velocity gradient as highlighted by the light blue colour (Fig. 13A). In Fig. 13A, the darker blue bands, indicating slightly negative velocity gradient, appeared alternatively with the bands of zero velocity gradient, albeit with lesser strength. Some large oscillation period $T(g/d_1)^{1/2} \sim 20$ ($T \sim 2 \text{ s}$) was observed for bands of negative velocity gradient during the unsteady gradually-varied flow phase.

The space-time variations of the fluctuations of velocity gradient tensor $\partial V_y/\partial z$ are shown in Fig. 13B. The velocity gradient fluctuations were calculated at each vertical elevation z at an instant t by taking the difference between the third and first quartiles (75–25% of the data

sample). For example, the fluctuation of the velocity gradient $\partial V_y/\partial z$ at time t is:

$$\left(\frac{\partial V_y}{\partial z}\right)_{fluc} = \left(\frac{\partial V_y}{\partial z}\right)_{75} - \left(\frac{\partial V_y}{\partial z}\right)_{25} \quad (9)$$

where the subscripts 75 and 25 denote the percentiles. For a data set with Gaussian distribution, the difference between the 75th and 25th percentiles is equivalent to 1.3 times the standard deviation. During the initially steady flow before the bore arrival, the majority of the vertical profile was associated with velocity gradient fluctuations between 16 s^{-1} and 25 s^{-1} , except for the upper one third of the profile and at the lower end of the profile. At the upper one third of the profile ($z/d_1 = 0.125\text{--}0.175$), low fluctuations were observed ($\sim 10\text{--}16 \text{ s}^{-1}$), as well as near the bottom of the profile, which was next to the channel bed ($z/d_1 < 0.025$).

When the breaking bore arrived, the velocity gradient fluctuations reacted with some time lag to the sudden change in flow. That is, the velocity fluctuations maintained the same space-time distributions as in the initially steady flow for a short period of time (dimensionless time ~ 10), before decreasing in magnitude. The time delay in reaction to the bore passage was approximately the same as the time span for the rapid flow deceleration. It implied that although the velocity gradient field changed drastically during the rapidly-varied flow phase, the field of velocity gradient fluctuations did not change as much. Another feature shown by the fluctuation data was the reaction time, which varied with different vertical elevations, as seen by Fig. 13B. Namely, it took longer for the velocity gradient fluctuations to react to the bore passage in the upper water column, compared to lower water column. Immediately after the rapid deceleration flow phase, the fluctuations in velocity gradient throughout the entire vertical profile decreased significantly, with a pocket of zero fluctuations occurring at dimensionless time > 126 and vertical elevations between $0.1 < z/d_1 < 0.175$ (purple colour).

The results in terms of velocity gradient tensor $\partial V_z/\partial y$ are shown in Fig. 14. A similar alternating pattern between slightly positive and negative gradient values was observed in the space-time variations before the bore arrival. With the bore passage, the velocity gradient fluctuated rapidly throughout the transverse profile. After the bore passage, the magnitudes of the velocity gradient tensor $\partial V_z/\partial y$ were smaller for the majority of the transverse profiles, and close to zero. The fluctuations of the velocity gradient tensor $\partial V_z/\partial y$ were consistently low (less than 25 s^{-1}) for the majority of the transverse profile in the initially steady flow. The propagation of the breaking bore caused the fluctuations to decrease with time, with different reaction times at different transverse locations. As the transverse distance y from the right sidewall increased, the velocity gradient fluctuations reacted less rapidly to the bore passage and started to decrease in magnitudes with a longer time delay. Overall, the ensemble-averaged space-time variations of the velocity gradient tensors $\partial V_y/\partial z$ and $\partial V_z/\partial y$ showed some similar trend, with comparable data range and fluctuation magnitudes.

6.2. Ensemble-averaged vorticity and strain rate

The present study conducted ensemble-averaged unsteady flow experiments using an array of two Profilers, with the two sampling profiles arranged orthogonal to each other. The two profiles had a point of intersection X, with the same y and z coordinate (Fig. 2C). At this intersection X, the vorticity around the longitudinal x axis and the strain rate in the y - z plane were calculated using Eqs. (5a) and (6b). Turbulent characteristics including enstrophy $\omega_x\omega_x$, enstrophy production rate $\omega_x S_{yz}\omega_x$, and the kinetic-energy dissipation rate $2\nu S_{yz}S_{yz}$ were derived from the vorticity and strain rate data. Since the flow field in breaking bores was highly turbulent and unsteady, all turbulent characteristics were analysed for three different flow phases: an initially steady flow phase before the bore arrival, followed by a rapidly-varying flow (rapid

deceleration) phase during which the free-surface rises abruptly, then an conjugate flow phase where the free-surface changes more gradually with large fluctuations.

Appendix II summarises the results in terms of the vorticity, strain rate, enstrophy, enstrophy production rate and kinetic-energy dissipation rate for the present study. The vorticity ω_x and strain rate S_{yz} were associated with both positive and negative values with a wide range of span, with an order of magnitude ranging from 10^{-2} s^{-1} to 10 s^{-1} , at different vertical elevations during different flow phases. The flow vorticity, at the intersection X, showed a tendency to decrease in magnitude with increasing vertical elevation, with the vorticity being negative, and largest in magnitude at the lowest vertical elevation. At the lowest vertical elevation and during different flow phases, the vorticity magnitudes increased in the rapidly-varied flow phase, compared to the initially steady flow phase. After the bore passage, the vorticity magnitudes decreased and became lower than during the steady flow phase, while staying negative throughout the three flow phases. The vorticity at the two higher vertical elevations fluctuated during the three flow phases. Since the vorticity at higher vertical elevations ranged from 10^0 s^{-1} to 10^{-2} s^{-1} in magnitude, hence the flow could be considered almost irrotational in the upper water column ($z/d_1 > 0.20$).

Fig. 15 shows a comparison of the vorticity ω_x and strain rate S_{yz} during different flow phases at different vertical elevations. A key feature highlighted by the results was that both vorticity and strain rate, at the intersection point X, were associated with largest magnitudes at the lowest vertical elevation. Further, both the vorticity and strain rate presented the largest magnitudes during the rapidly-varied flow phase at the lowest vertical elevation. The results suggested: (a) the flow before, during and after the bore propagation was highly turbulent, with intensive vortex motions occurring mostly in the lower water column; (b) the passage of breaking bore caused the flow to rapidly decelerate, which induced the formation of energetic vortical structures and amplified the vortical motion at the lower vertical elevations.

7. Discussion

Khezri [19] conducted 2D CFD modelling of breaking bores propagating in open channel flows and documented vorticity fields beneath the bore and in the initially steady flow. Her data showed vorticity ω_y ranging from 0 to -150 s^{-1} beneath the bore front very close to the bed ($z/d_1 = 0$). Despite the difference in the axis of rotation, the results agreed in terms of order of magnitude with the present study. Further, Khezri [19] observed large vortical structures forming next to the bed underneath the toe of the breaking bore, with a vertical dimension close to the initial steady flow depth. The vorticity decreased with increasing vertical elevation and increased with the passage of the breaking bore [19]. With undular bores, 3D CFD modelling showed vorticity ω_y ranging from -20 s^{-1} to 50 s^{-1} throughout the water column [32]. The magnitude in vorticity decreased with increasing vertical elevation and increased as the bore front propagated passed the probing point.

In summary, the present study agreed qualitatively and quantitatively with past CFD numerical data [19,32,25] in terms of order of magnitude.

8. Conclusion

The unsteady turbulent properties of a compression wave propagating in an open channel were measured physically under controlled flow conditions. Using an array of two Profiler velocimeters, installed perpendicular to each other, in a large-size laboratory flume (19 m long, 0.7 m wide), two-dimensional space-time correlations were performed in the y - z plane. The turbulent time and length scales were deduced for the different flow phases of a compression wave.

The two-dimensional cross-correlation data in the y - z plane, formed

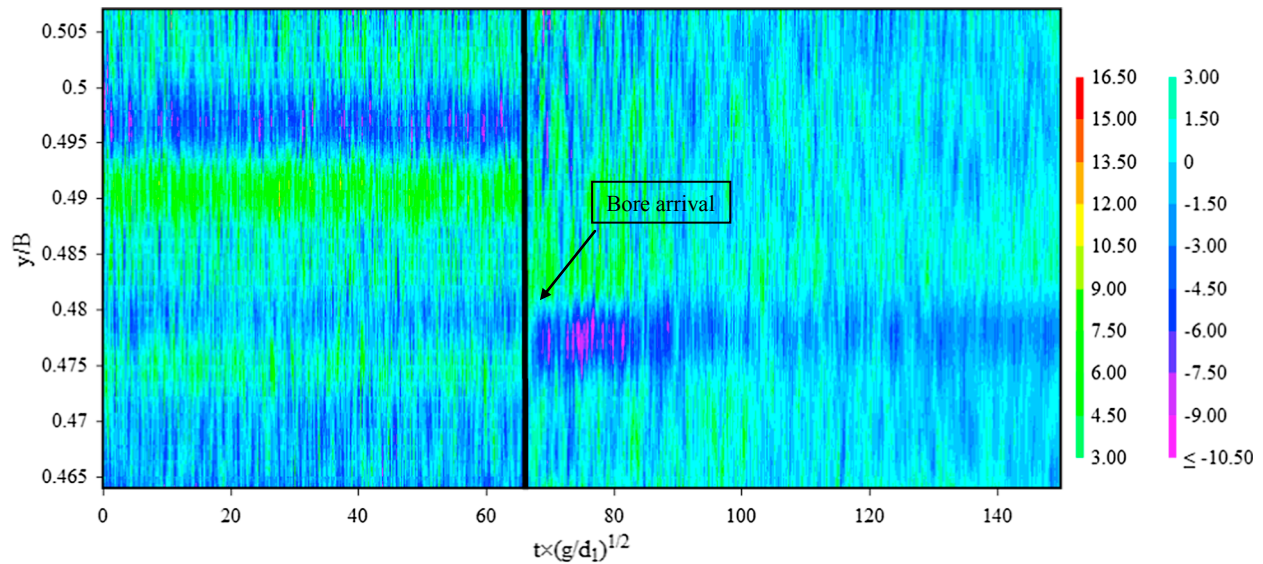
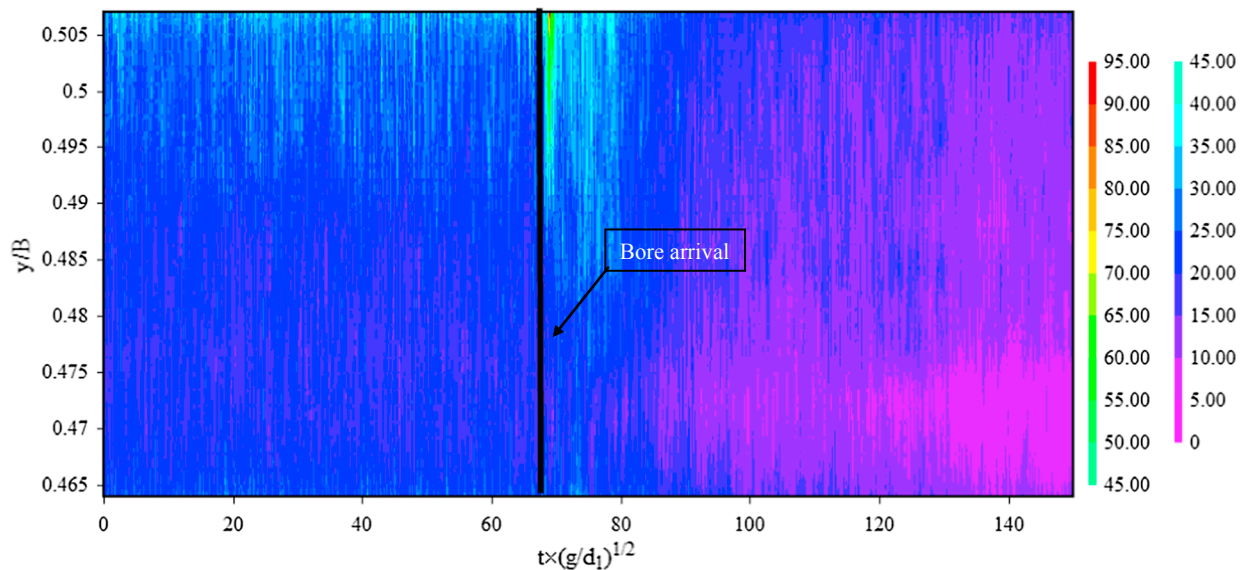
(A) Space-time contour of the ensemble-averaged velocity gradient tensor $\partial V_z/\partial y$ (s^{-1})(B) Space-time contour of the velocity gradient fluctuation of tensor component $\partial V_z/\partial y$ (s^{-1})

Fig. 14. Space-time contour of the ensemble-averaged velocity gradient and velocity gradient fluctuations of tensor component $\partial V_z/\partial y$ during the propagation of breaking bores – Flow conditions: $Q = 0.101 \text{ m}^3/\text{s}$, $d_1 = 0.174 \text{ m}$, $Fr_1 = 1.52$, $z/d_1 = 0.00\text{--}0.20$, $y/B = 0.46\text{--}0.51$.

by the two sampling profiles of the Profiler array, showed the existence of large scale coherent structures underneath the free-surface. These structures usually formed in pairs, with a cross-sectional shape in the y - z plane similar to that of some hair-pin vortex. The transverse and vertical length scales of such structures ranged from 0.01 to 0.05 times the channel width. The length scales tended to increase during and after the bore passage, compared to those during the initially steady flows. With simultaneous velocity measurements conducted in the transverse y and vertical z directions, the vorticity and strain rate were determined experimentally, at the point of intersection of the two sampling profiles. Both strain rate and vorticity reached maximum values in the lower water column next to the channel bed, and during the rapid deceleration associated with the compression wave passage. The results suggested the formation of large-scale coherent structures next to the channel bed caused by boundary shearing, followed by break-up into smaller structures/eddies as the vortices travelled upward into the

water column, in the initially steady flow. When the flow became unsteady and rapidly-varied with the passage of the compression wave, larger vortical structures were created and the vortical motion next to the bed was amplified.

In summary, the results overall suggested that the propagation of compression waves is a dynamically-active process, with the existence of large scale coherent motions, vortical structures and intense turbulent mixing occurring underneath. The work showed the potential of an array of two ADV Profilers to gain a deeper insight into the transient turbulence characteristics in an unsteady rapidly varied open channel flow.

Acknowledgments

The authors thank Dr Bruce Macvicar (University of Waterloo, Canada) and Dr Colin Rennie (University of Ottawa, Canada) for

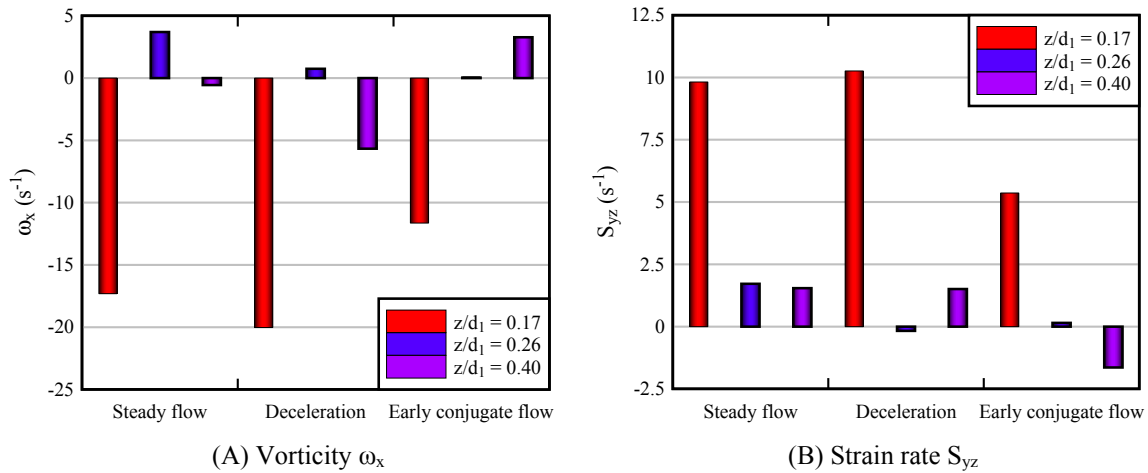


Fig. 15. Comparison of vorticity ω_x and strain rate S_{yz} during different flow phases (steady flow, rapidly-varied flow and conjugate flow) at the intersection points X with locations $y/B = 0.5$, $z/d_1 = 0.17, 0.26$ and 0.40 .

valuable comments. The authors thank Professor Pierre Lubin (University of Bordeaux, France) for his personal involvement, contribution and comments, as well as Dr Hang Wang (The University of Queensland, Brisbane) for his encouragements. The authors acknowledge the technical contribution of Dr Jan Becker (Federal Waterways Engineering and Research Institute, Germany) and Gangfu Zhang (The University of Queensland, Australia) in the data post-processing program. The authors also acknowledge the technical assistance of Jason

Van Der Gevel, Stewart Matthews and Dr Van Thuan Nguyen (The University of Queensland). The financial support through the Australian Research Council (Grant DP120100481) is acknowledged.

Declaration of interest

The authors have no conflict of interest nor vested interests. This is not an industry sponsored study.

Appendix I. Turbulent area scale and associated integral time scale in the y-z plane.

Reference	S_o	Q (m^3/s)	d_1 (m)	h (m)	z/d_1	y/B	Fr_1	X location
1a	0	0.101	0.174	0	0.01–0.20	0.46–0.51	1.52	$z/d_1 = 0.17y/B = 0.50$
1b	0	0.101	0.176	0	0.09–0.28	0.46–0.51	1.5	$z/d_1 = 0.26y/B = 0.50$
1c	0	0.101	0.176	0	0.23–0.43	0.46–0.51	1.55	$z/d_1 = 0.40y/B = 0.50$

Ref.	Steady				Rapid				Deceleration				Conjugate flow					
	$A_{yz,x}$ (mm^2)	$T_{yz,x}$ (s)	$A_{yz,y}$ (mm^2)	$T_{yz,y}$ (s)	$A_{yz,z}$ (mm^2)	$T_{yz,z}$ (s)	$A_{yz,x}$ (mm^2)	$T_{yz,x}$ (s)	$A_{yz,y}$ (mm^2)	$T_{yz,y}$ (s)	$A_{yz,z}$ (mm^2)	$T_{yz,z}$ (s)	$A_{yz,x}$ (mm^2)	$T_{yz,x}$ (s)	$A_{yz,y}$ (mm^2)	$T_{yz,y}$ (s)	$A_{yz,z}$ (mm^2)	$T_{yz,z}$ (s)
1a	54.6	0.048	130.18	0.017	47.41	0.016	60.26	0.029	<i>0.34</i>	<i>0.017</i>	<i>0</i>	<i>0</i>	162.07	0.194	227.1	0.210	<i>0</i>	<i>0</i>
1b	26.71	0.031	139.69	0.011	37.53	0.016	36.34	0.019	11.89	0.007	<i>0</i>	<i>0</i>	191.84	0.197	88.08	0.116	<i>0</i>	<i>0</i>
1c	4.61	0.070	129.56	0.009	46.23	0.019	63.68	0.027	<i>0.42</i>	<i>0.022</i>	<i>0.84</i>	<i>0.02</i>	130.64	0.130	77.64	0.134	90.73	0.134

Note: *Italic input*: suspicious data.

Appendix II. Ensemble-averaged vorticity, strain rate, enstrophy, enstrophy production rate, and the kinetic-energy dissipation rate at the intersection X of the sampling profiles measured by an array of two Profilers in a compressive wave with a breaking roller.

Reference	Steady					Rapid			deceleration			Conjugate flow				
	ω_x (s^{-1})	S_{yz} (s^{-1})	$\omega_x S_{yz} \omega_x$ (s^{-3})	$2\nu S_{yz} S_{yz}$ ($m^2 s^{-3}$)	$\omega_x \omega_x$ (s^{-2})	ω_x (s^{-1})	S_{yz} (s^{-1})	$\omega_x S_{yz}$ (s^{-2})	$2\nu S_{yz} S_{yz}$ ($m^2 s^{-3}$)	$\omega_x \omega_x$ (s^{-2})	ω_x (s^{-1})	S_{yz} (s^{-1})	$\omega_x S_{yz} \omega_x$ (s^{-3})	$2\nu S_{yz} S_{yz}$ ($m^2 s^{-3}$)	$\omega_x \omega_x$ (s^{-2})	
1a	-17.31	9.82	2943.57	1.93×10^{-4}	299.80	-20.03	10.26	4116.07	2.10×10^{-4}	401.27	-11.64	5.36	725.31	5.74×10^{-5}	135.43	
1b	3.70	1.72	23.56	5.93×10^{-6}	13.69	0.75	-0.17	-0.10	5.90×10^{-8}	0.57	0.03	0.15	0.00	4.22×10^{-8}	0.00	
1c	-0.56	1.54	0.49	4.76×10^{-6}	0.32	-5.67	1.51	48.56	4.57×10^{-6}	32.14	3.28	-1.64	-17.59	5.37×10^{-6}	10.73	

Notes: The experimental conditions corresponding to references 1a, 1b and 1c are detailed in Table 1; For all turbulent statistics in the table, the data were averaged over 60 s during the steady flow phase, over 1–3 s during the rapid deceleration phase starting at the initiation of flow deceleration, and over 10 s for the early conjugate flow phase starting at the end of the rapid deceleration phase.

Appendix B. Supplementary material

Supplementary data to this article can be found online at <https://doi.org/10.1016/j.expthermflusci.2018.09.014>.

References

- [1] S. Abadie, J.C. Harris, S.T. Grilli, R. Fabre, numerical modeling of tsunami waves generated by the flank collapse of the cumbre vieja volcano (la palma, canary islands): tsunami source and near field effects, *J. Geophys. Res. C: Oceans*, AGU 117 (5) (2012) C05030.
- [2] R.J. Adrian, Hairpin vortex organization in wall turbulence, *Phys. Fluids* 19 (2008) Paper 041301.
- [3] H. Bazin, Recherches Expérimentales sur la Propagation des Ondes. ('Experimental Research on Wave Propagation'.) Mémoires présentés par divers savants à l'Académie des Sciences Paris, France, Vol. 19 (1865) pp. 495–644 (in French).
- [4] J. Becker, VTMT (Version 1.1) [Computer software]. Federal Waterways Engineering and Research Institute (BAW), Karlsruhe, 2014. Retrieved from <http://sdrv.ms/12eHgvw/>.
- [5] F. Benet, J.A. Cunge, Analysis of experiments on secondary undulations caused by surge waves in trapezoidal channels, *J. Hydraul. Res., IAHR* 9 (1) (1971) 11–33.
- [6] B.J. Cantwell, On the behavior of velocity gradient tensor invariants in direct numerical simulations of turbulent, *Phys. Fluids A* 5 (8) (1993) 2008–2013, <https://doi.org/10.1063/1.858828>.
- [7] H. Chanson, Acoustic Doppler velocimetry (ADV) in the field and in laboratory: practical experiences, in: Proceedings of the International Meeting on Measurements and Hydraulics of Sewers IMMHS'08, Summer School GEMCEA/LCPC, 19–21 Aug. 2008, Bouguenais, Frédérique LARRARTE and Hubert CHANSON Eds., Hydraulic Model Report No. CH70/08, Div. of Civil Engineering, The University of Queensland, Brisbane, Australia, Dec., 2008, pp. 49–66.
- [8] H. Chanson, Unsteady turbulence in compression waves: effects of bed roughness, *J. Waterw. Port Coastal Ocean Eng., ASCE* 136 (5) (2010) 247–256, [https://doi.org/10.1061/\(ASCE\)WW.1943-5460.0000048](https://doi.org/10.1061/(ASCE)WW.1943-5460.0000048).
- [9] H. Chanson, Tidal Bores, Aegir, Eagre, Mascaret, Pororoca: Theory and Observations, World Scientific, Singapore, 2011, p. 220 (ISBN 9789814335416).
- [10] H. Chanson, Applied Hydrodynamics: An Introduction, CRC Press, Taylor & Francis Group, Leiden, The Netherlands, 2014, p. 448 21 video movies (ISBN 978-1-138-00093-3).
- [11] H. Chanson, P. Lubin, Mixing and Sediment Processes induced by Tsunamis propagating Upriver, Chapter 3 Nova Science Publishers, Hauppauge NY, USA, 2013, pp. 65–102.
- [12] R.G.A. Craig, C. Loadman, B. Clement, P.J. Ruesello, E. Siegel, Characterization and testing of a new bistatic profiling acoustic doppler velocimeter: the vectrino-II, in: Proc. IEEE/OES/CWTM 10th Working Conference on Current, Waves and Turbulence Measurement (CWTM), Monterey, Canada, 20–23 March, 2011, pp. 246–252 10.1109/CWTM.2011.5759559.
- [13] S. Dilling, B. Macvicar, Cleaning high-frequency velocity profile data with autoregressive moving average (ARMA) models, *Flow Meas. Instrum.* 54 (2017) 68–81.
- [14] H. Favre, Etude Théorique et Expérimentale des Ondes de Translation dans les Canaux Découverts, Theoretical and Experimental Study of Travelling Surges in Open Channels, Dunod, Paris, France, 1935 (in French).
- [15] A.J. Favre, Review on space-time correlations in turbulent fluids, *J. Appl. Mech. ASME*. 32 (2) (1965) 241–257, <https://doi.org/10.1115/1.3625792>.
- [16] D.G. Goring, V.I. Nikora, Despiking acoustic Doppler velocimeter data, *J. Hydraul. Eng., ASCE* 128 (1) (2002) 117–126 Discussion: Vol. 129, No. 6, pp. 484–489.
- [17] J.O. Hinze, Turbulence. McGraw-Hill Publ, second ed., New York, USA, 1975.
- [18] H.G. Hornung, C. Willert, S. Turner, the flow field downstream of a hydraulic jump, *J. Fluid Mech.* 287 (1995) 299–316.
- [19] N. Khezri, Modelling turbulent mixing and sediment process beneath compression waves: physical and numerical investigations, Ph.D. thesis, School of Civil Engineering, The University of Queensland, Brisbane, Australia, 2014, 267 pages.
- [20] C. Koch, H. Chanson, Turbulent mixing beneath an undular bore front, *J. Coastal Res.* 24 (4) (2008) 999–1007, <https://doi.org/10.2112/06-0688.1>.
- [21] C. Koch, H. Chanson, Turbulence measurements in positive surges and bores, *J. Hydraul. Res., IAHR* 47 (1) (2009) 29–40, <https://doi.org/10.3826/jhr.2009.2954>.
- [22] X. Leng, H. Chanson, Turbulent advances of a breaking bore: preliminary physical experiments, *Exp. Therm Fluid Sci.* 62 (2015) 70–77, <https://doi.org/10.1016/j.expthermflusci.2014.12.002>.
- [23] X. Leng, H. Chanson, integral turbulent scales in unsteady rapidly varied open channel flows, *Exp. Therm Fluid Sci.* 81 (2017) 382–395, <https://doi.org/10.1016/j.expthermflusci.2016.09.017>.
- [24] X. Leng, H. Chanson, simultaneous velocity profiling in unsteady turbulent flows using an array of two vectrino profilers, Hydraulic Model Report No. CH106/17, School of Civil Engineering, The University of Queensland, Brisbane, Australia, 2018, 134 pages.
- [25] X. Leng, B. Simon, N. Khezri, P. Lubin, H. Chanson, CFD modelling of tidal bores: development and validation challenges, *Coastal Eng. J.* 14 (2017) pages, <https://doi.org/10.1080/21664250.2018.1498211>.
- [26] B.J. McKeon, G. Comte-bellot, J.F. Foss, J. Westerweel, F. Scarano, C. Tropea, J.F. Meyers, J.W. Lee, A.A. Cavone, R. Schodl, M.M. Koochesfahani, D.G. Nocera, Y. Andreopoulos, W.J.A. Dahm, J.A. Mullin, J.M. Wallace, P.V. Vukoslavcevic, S.C. Morris, E.R. Pardyjak, A. Cuerva, Nondimensional representation of the boundary-value problem, Part A, Chapter 2 Springer, Heidelberg, Germany, 2007, pp. 33–83.
- [27] Macvicar, B., Dilling, S., Lacey, J., and Hipel, K. (2014). "A Quality Analysis of the Vectrino II Instrument using a New Open-source MATLAB Toolbox and 2D ARMA Models to Detect and Replace Spikes." Proc. 7th International Conference on Fluvial Hydraulics (River Flow), Lausanne, Switzerland, 3–5 Sept., 2014, pp. 1951–1959.
- [28] H. Nakagawa, I. Nezu, Structure of space-time correlations of bursting phenomena in an open-channel flow, *J. Fluid Mech.* 104 (1981) 1–43, <https://doi.org/10.1017/S0022112081002796>.
- [29] V. Nikora, Personnel Communication on the suitability of ADV despiking techniques in rapidly-varied unsteady flows, 2004.
- [30] Nortek, Vectrino Profiler: User Guide, Nortek Scientific Acoustic Development Group Inc., User Manual, 2012.
- [31] N. Shuto, The Nihonkai-Chubu earthquake Tsunami on the North Akita coast, *Coast. Eng. Jpn.* 20 (1985) 250–264.
- [32] B. Simon, Effects of compression waves on turbulent mixing: a numerical and physical study in positive surges, Ph.D. thesis, School of Civil Engineering, The University of Queensland, Brisbane, Australia, 2014, 259 pages & 7 movies.
- [33] J.J. Stoker, Water Waves. The mathematical Theory with Applications, Interscience Publishers, New York, USA, 1957, p. 567.
- [34] T. Theodorsen, Mechanism of turbulence, in: Proceedings of the Midwestern Conference Fluid Mechanics, Ohio State University, Columbus, 1952, pp. 1–19.
- [35] A. Treske, Undular bores (favre-waves) in open channels – experimental studies, *J. Hyd. Res., IAHR* 32 (3) (1994) 355–370 Discussion: Vol. 33, No. 3, 1994, pp. 274–278.
- [36] R.A.R. Tricker, Bores, Breakers, Waves and Wakes, American Elsevier Publ. Co., New York, USA, 1965.
- [37] J.M. Wallace, Highlights from 50 years of turbulent boundary layer research, *J. Turbul.* 13 (53) (2013) 1–70.
- [38] L. Zedel, A. Hay, Turbulence measurements in a jet: comparing the vectrino and vectrino II, in: Proc. IEEE/OES/CWTM 10th Working Conference on Current, Waves and Turbulence Measurements (CWTM), Monterey, Canada, 20–23 March, 2011, pp. 173–178 10.1109/CWTM.2011.5759547.
- [39] J. Zhou, R.J. Adrian, S. Balachandar, T.M. Kendall, Mechanisms for generating coherent packets of hairpin vortices in channel flow, *J. Fluid Mech.* 387 (1999) 353–396.